



**NAVAL
POSTGRADUATE
SCHOOL**

MONTEREY, CALIFORNIA

THESIS

**EXPLORATION OF DATA FUSION BETWEEN
POLARIMETRIC RADAR AND MULTISPECTRAL IMAGE
DATA**

by

William D. Hall

September 2012

Thesis Advisor:
Second Reader:

Fred A. Kruse
Brett Borden

Approved for public release; distribution is unlimited

THIS PAGE INTENTIONALLY LEFT BLANK

REPORT DOCUMENTATION PAGE		Form Approved OMB No. 0704-0188	
Public reporting burden for this collection of information is estimated to average 1 hour per response, including the time for reviewing instruction, searching existing data sources, gathering and maintaining the data needed, and completing and reviewing the collection of information. Send comments regarding this burden estimate or any other aspect of this collection of information, including suggestions for reducing this burden, to Washington headquarters Services, Directorate for Information Operations and Reports, 1215 Jefferson Davis Highway, Suite 1204, Arlington, VA 22202-4302, and to the Office of Management and Budget, Paperwork Reduction Project (0704-0188) Washington DC 20503.			
1. AGENCY USE ONLY (Leave blank)	2. REPORT DATE September 2012	3. REPORT TYPE AND DATES COVERED Master's Thesis	
4. TITLE AND SUBTITLE Exploration of Data Fusion between Polarimetric Radar and Multispectral Image Data		5. FUNDING NUMBERS N/A	
6. AUTHOR(S) William D. Hall		8. PERFORMING ORGANIZATION REPORT NUMBER N/A	
7. PERFORMING ORGANIZATION NAME(S) AND ADDRESS(ES) Naval Postgraduate School Monterey, CA 93943-5000		10. SPONSORING/MONITORING AGENCY REPORT NUMBER N/A	
9. SPONSORING /MONITORING AGENCY NAME(S) AND ADDRESS(ES) N/A		11. SUPPLEMENTARY NOTES The views expressed in this thesis are those of the author and do not reflect the official policy or position of the Department of Defense or the U.S. Government. IRB Protocol number: N/A.	
12a. DISTRIBUTION / AVAILABILITY STATEMENT Approved for public release; distribution is unlimited		12b. DISTRIBUTION CODE A	
13. ABSTRACT (maximum 200 words) Typically, analysis of remote sensing data is limited to one sensor at a time which usually contains data from the same general portion of the electromagnetic spectrum. SAR and visible near infrared data of Monterey, CA, were analyzed and fused with the goal of achieving improved land classification results. A common SAR decomposition, the Pauli decomposition was performed and inspected. The SAR Pauli decomposition and the multispectral reflectance data were fused at the pixel level, then analyzed using multispectral classification techniques. The results were compared to the multispectral classifications using the SAR decomposition results for a basis of interpreting the changes. The combined dataset resulted in little to no quantitative improvement in land cover classification capability, however inspection of the classification maps indicated an improved classification ability with the combined data. The most noticeable increases in classification accuracy occurred in spatial regions where the land features were parallel to the SAR flight line. This dependence on orientation makes this fusion process more ideal for datasets with more consistent features throughout the scene.			
14. SUBJECT TERMS SAR Radar Multispectral Imagery Data Fusion UAVSAR WorldView-2 WV-2		15. NUMBER OF PAGES 85	
		16. PRICE CODE	
17. SECURITY CLASSIFICATION OF REPORT Unclassified	18. SECURITY CLASSIFICATION OF THIS PAGE Unclassified	19. SECURITY CLASSIFICATION OF ABSTRACT Unclassified	20. LIMITATION OF ABSTRACT UU

THIS PAGE INTENTIONALLY LEFT BLANK

Approved for public release; distribution is unlimited

**EXPLORATION OF DATA FUSION BETWEEN POLARIMETRIC
AND MULTISPECTRAL IMAGE DATA**

William D. Hall
Civilian, Department of the Navy
B.S., California State University at Stanislaus, 2011

Submitted in partial fulfillment of the
requirements for the degree of

MASTER OF SCIENCE IN REMOTE SENSING INTELLIGENCE

from the

**NAVAL POSTGRADUATE SCHOOL
September 2012**

Author: William D. Hall

Approved by: Dr. Fred A. Kruse
Thesis Advisor

Dr. Brett Borden
Second Reader

Dr. Dan Boger
Chair, Department of Information Sciences

THIS PAGE INTENTIONALLY LEFT BLANK

ABSTRACT

Typically, analysis of remote sensing data is limited to one sensor at a time which usually contains data from the same general portion of the electromagnetic spectrum. SAR and visible near infrared data of Monterey, CA, were analyzed and fused with the goal of achieving improved land classification results. A common SAR decomposition, the Pauli decomposition was performed and inspected. The SAR Pauli decomposition and the multispectral reflectance data were fused at the pixel level, then analyzed using multispectral classification techniques. The results were compared to the multispectral classifications using the SAR decomposition results for a basis of interpreting the changes. The combined dataset resulted in little to no quantitative improvement in land cover classification capability, however inspection of the classification maps indicated an improved classification ability with the combined data. The most noticeable increases in classification accuracy occurred in spatial regions where the land features were parallel to the SAR flight line. This dependence on orientation makes this fusion process more ideal for datasets with more consistent features throughout the scene.

THIS PAGE INTENTIONALLY LEFT BLANK

TABLE OF CONTENTS

I.	INTRODUCTION	1
A.	OBJECTIVES	3
II.	BACKGROUND	5
A.	RADIATIVE TRANSFER FUNDAMENTALS	5
1.	Electromagnetic Theory	5
B.	MULTISPECTRAL IMAGING	10
C.	SAR IMAGING	11
D.	WORLDVIEW-2 SATELLITE IMAGERY	13
E.	UNINHABITED AERIAL VEHICLE SYNTHETIC APERTURE RADAR (UAVSAR)	15
F.	IMAGE CLASSIFICATION	17
1.	Supervised Classification Methods	17
2.	Pauli Decomposition	22
3.	Data Fusion	24
III.	METHODS	27
A.	FLAASH ATMOSPHERIC CORRECTION	27
B.	REGISTRATION	28
C.	WV-2 CLASSIFICATION	30
D.	PAULI DECOMPOSITION COMPUTATION AND FUSION	33
IV.	RESULTS	37
V.	CONCLUSIONS	55
	APPENDIX: ADDITIONAL RESULTS FIGURES AND TABLES	57
	LIST OF REFERENCES	61
	INITIAL DISTRIBUTION LIST	67

THIS PAGE INTENTIONALLY LEFT BLANK

LIST OF FIGURES

Figure 1.	The electromagnetic spectrum (From Wikimedia Commons file "Image: Electromagnetic-Spectrum.png," retrieved June 1, 2012).....	6
Figure 2.	The three possible polarization states: linear polarization (top), circular polarization (middle), and elliptical polarization (bottom) (From Chai, 2011).....	9
Figure 3.	Polarization ellipse(From MacDonald, 1999).....	10
Figure 4.	WV-2 Dataset. Red box outlines subset used for this study.....	15
Figure 5.	UAVSAR dataset.....	16
Figure 6.	Example Pauli decomposition image of the San Francisco, California, area (From Lee & Pottier, 2009).....	23
Figure 8.	WV-2 true color image of the Monterey subset with ROIs overlaid.....	31
Figure 9.	Urban ROI mean/min/max spectra (left) and sample pixel spectra (right).....	32
Figure 10.	WV-2 data with reference ROIs overlaid.....	33
Figure 11.	Pauli decomposition image.....	34
Figure 12.	Classification image ROI key.....	37
Figure 13.	MSI Mahalanobis distance classification.....	38
Figure 14.	MSI maximum likelihood classification.....	39
Figure 15.	MSI minimum distance classification.....	40
Figure 16.	SAR maximum likelihood classification image.....	46
Figure 17.	MSI+SAR Mahalanobis distance classification image.....	48
Figure 18.	MSI+SAR maximum likelihood classification image.....	49
Figure 19.	MSI+SAR minimum distance classification image...	50
Figure 20.	SAR Mahalanobis distance classification.....	57
Figure 21.	SAR minimum distance classification image.....	58

THIS PAGE INTENTIONALLY LEFT BLANK

LIST OF TABLES

Table 1.	Sample confusion matrix (From Monserud, 1992)...	19
Table 2.	Example confusion matrix.....	20
Table 3.	Kappa coefficients and their degree of agreement (From Monserud, 1992).....	22
Table 4.	Confusion matrix legend.....	40
Table 5.	MSI Mahalanobis distance confusion matrix.....	41
Table 6.	MSI Mahalanobis distance user/prod. acc.....	42
Table 7.	MSI maximum likelihood distance confusion matrix.....	43
Table 8.	MSI maximum likelihood user/prod. acc.....	43
Table 9.	MSI minimum distance confusion matrix.....	44
Table 10.	MSI minimum distance user/prod. acc.....	44
Table 11.	SAR maximum likelihood confusion matrix.....	46
Table 12.	SAR maximum likelihood user/prod. acc.....	47
Table 13.	MSI+SAR Mahalanobis distance confusion matrix...	51
Table 14.	MSI+SAR Mahalanobis distance user/prod. acc.....	51
Table 15.	MSI+SAR maximum likelihood confusion matrix.....	52
Table 16.	MSI+SAR maximum likelihood user/prod. acc.....	53
Table 17.	MSI+SAR minimum distance confusion matrix.....	53
Table 18.	MSI+SAR minimum distance user/prod. acc.....	54
Table 19.	Results summary table.....	54
Table 20.	SAR Mahalanobis distance confusion matrix.....	57
Table 21.	SAR Mahalanobis distance user/prod. acc.....	58
Table 22.	SAR minimum distance confusion matrix.....	59
Table 23.	SAR minimum distance user/prod. acc.....	59

THIS PAGE INTENTIONALLY LEFT BLANK

LIST OF ACRONYMS AND ABBREVIATIONS

EM	ElectroMagnetic
FLAASH	Fast-line-of-sight Atmospheric Analysis of Spectral Hypercubes
GCP	Ground Control Point
IHS	Intensity-Hue-Saturation
IR	InfraRed
MODTRAN	MODerate resolution atmospheric TRANsmission SAR Synthetic Aperture Radar
MSI	MultiSpectral Imagery
MSS	MultiSpectral Scanner
NIR	Near InfraRed
RGB	Red, Green, Blue
ROI	Region Of Interest
VNIR	Visible and Near InfraRed
WV-2	WorldView-2

THIS PAGE INTENTIONALLY LEFT BLANK

ACKNOWLEDGMENTS

The author would like to thank the entire staff of the Remote Sensing Center at the Naval Postgraduate School for making my education possible.

The author wishes to extend a special thanks to Krista Lee and Chad Brodel Ph.D. from among this staff for helping me both personally and academically during my time at the Naval Postgraduate School.

As well, none of this would have been possible without the efforts and dreams of Professor Richard C. Olsen towards creation of this program.

The author would also like to thank Professor Fred A. Kruse for his patience and insight during the thesis process.

THIS PAGE INTENTIONALLY LEFT BLANK

I. INTRODUCTION

Land cover classification applications of remote sensing exist in many fields, including but not limited to: civil planning, agriculture, forestry, and tactical military operations. Civil engineers faced with rapid urbanization and population growth need to obtain information about ground cover and type to adequately handle urban sprawl (Thunig et al., 2011). It has been shown that data fusion from multiple sensors of different spatial resolutions can be performed to increase the dimensionality of the vectors being classified. This approach has resulted in demonstrations of improved classification accuracy (Kempeneers et al., 2011).

Remote sensing applications range from specific material identification using hyperspectral imaging (spectral/spatial imaging in many contiguous spectral bands), to elevation mapping, to terrain classification mapping. Sensors come in many varieties with a wide range of spectral bands, ground sample distances, revisit times, and many other features. New applications for existing technologies are not uncommon in the field, as the potential for remote sensors is often far greater than imagined during the design stages.

Data fusion is the concept of combining data from multiple sources, (i.e., imaging radar and electro optical multispectral sensors) in order to simultaneously exploit their individual phenomenologies. The goal of this approach is to increase identification or detection abilities and the confidence levels of both. It is expected that

employing both systems will reveal more information about a scene than either system is capable of independently. Finding new ways to synchronize these data should increase the information gain provided by this synthesis.

Early work in synthetic aperture radar (SAR)/electro optical multispectral data fusion began in 1980 with the combination of airborne SAR data, an airborne multispectral scanner, and Landsat data (Guindon et al., 1980). The classification results did not improve in this first attempt at data fusion over a single airborne Multispectral Scanner (MSS). In 1982, Seasat L-band and airborne X-band SAR data were fused with Landsat multispectral scanner (MSS) data to classify land cover type (Wu, 1982). This work did show improved classification results however, unlike the work in this document, unsupervised classification techniques were used. In 1990 visible and near infrared (VNIR) MSS and SAR data were used to classify different vegetation species, densities, and even different ages of the same species successfully (Leckie, 1990). Many different combinations of subsets of all the data were tested and it was found that many different unique combinations were the most successful discriminators of certain classes. In 2011, airborne SAR and airborne optical images were combined to classify land cover types with a combined classification accuracy and Kappa coefficient of 94% and 0.92 respectively (Liu et al., 2011). Similar to the work in this document, maximum likelihood classification was used. In 2012 it was demonstrated that the fusion of SAR and optical data could be used to calculate soil moisture with high accuracy (Prakash and Singh, 2012). The optical data were used to create a land

cover mask of the area and the additional SAR information related to the NDVI to calculate soil moisture.

A. OBJECTIVES

The primary objective of this work was to achieve improved land cover classification accuracy by using two datasets of the same geographic area from different portions of the electromagnetic spectrum.

In this research, multispectral data from DigitalGlobe's WorldView-2 (WV-2) satellite were used to classify land cover types for a portion of Monterey, CA. Data acquired by the Uninhabited Aerial Vehicle Synthetic Aperture Radar (UAVSAR) were also analyzed, and the two datasets were fused for combined analysis. The fused VNIR and Radar information were used to classify the scene and the results were compared to the classification from the WV-2 data only. Classification results were expected to improve, however, due to spectral variability within the scene and large pixel sizes in the SAR data, classification improvements were nil to marginal.

THIS PAGE INTENTIONALLY LEFT BLANK

II. BACKGROUND

A. RADIATIVE TRANSFER FUNDAMENTALS

1. Electromagnetic Theory

Electromagnetic (EM) radiation is a form of energy that is emitted and absorbed by charged particles. This radiation is composed of electric and magnetic fields which oscillate in-phase perpendicular to each other and the direction of wave propagation. The energy is characterized by the frequency of these oscillations. The collection of frequencies is known as the electromagnetic spectrum (Olsen, 2007). Figure 1 shows the names and associated frequencies and wavelengths of important portions of the electromagnetic spectrum (Kleeman, 1930; Olsen, 2007).

Electromagnetic radiation can be described as a stream of photons (massless particles moving at the speed of light in a wavelike pattern)(Kleeman, 1930). The photons have energy related to the frequency of their wave pattern as shown in equation 1.1,

$$E = \frac{hc}{\lambda} \qquad \text{Equation 1.1}$$

where $c=2.99 \times 10^8$ m/s is the speed of light, and $h=6.626 \times 10^{-34}$ kg/s is Planck's constant (Olsen, 2007).

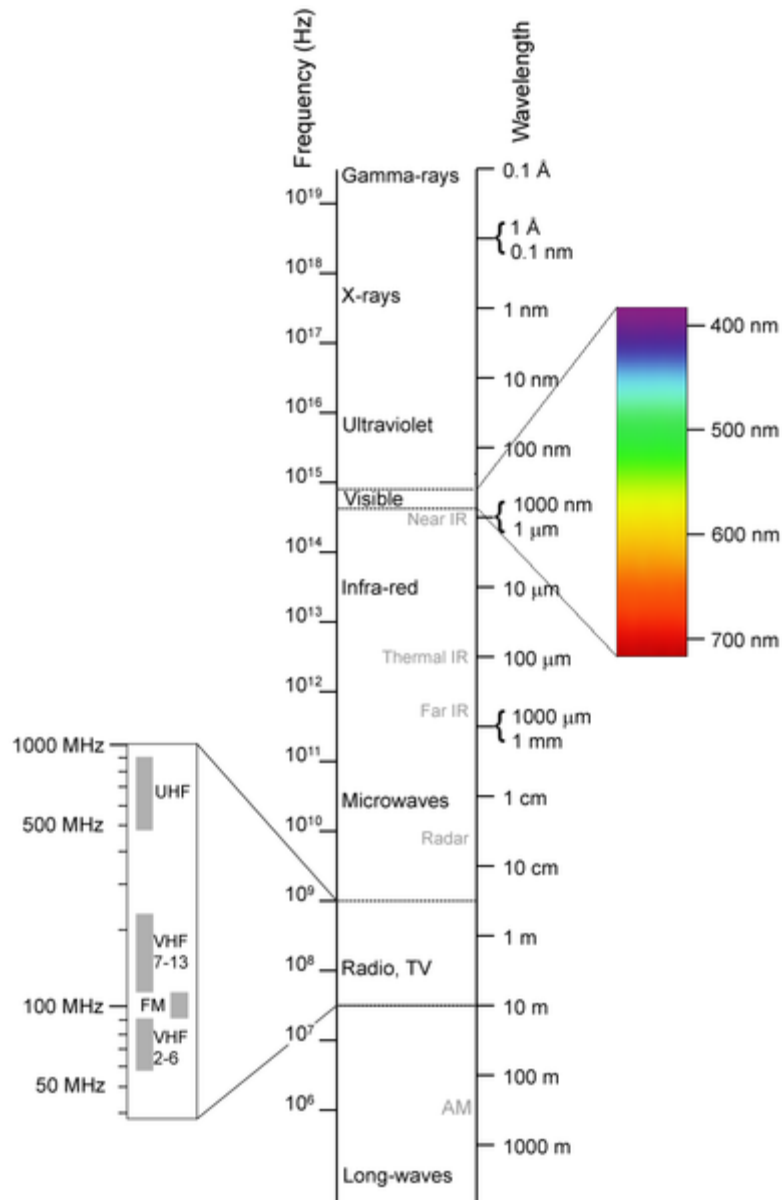


Figure 1. The electromagnetic spectrum (From Wikimedia Commons file "Image: Electromagnetic-Spectrum.png," retrieved June 1, 2012)

Remote sensing utilizes detection of the phenomena of the interactions between materials and electromagnetic energy at different wavelengths in the spectrum without actual contact with the materials (Elachi, 1987). Commonly used portions of the spectrum for imaging purposes include

but are not limited to: visible light (.4-.8 micrometers), near infrared (.8-2.5 micrometers), and microwave (usually Radar) (1cm - 1m). For electro optical systems, photons are collected on sensor arrays that are calibrated to certain wavelength ranges. The measured intensity value recorded by a sensor represents the number of photons collected and is recorded as a digital number. Measurements are often taken across an entire scene and compiled to create a dataset that is displayable as an image (Lulla and Jensen, 1987).

Remote sensing detects electromagnetic radiation that has interacted with the materials being observed in some way (scattered, transmitted, emitted, or reflected). Usually this is done by measuring the amplitude of the energy at certain wavelengths. Beyond amplitude, EM waves also carry polarization information, which can be used to provide addition information. Spectral information gives information about the materials being imaged, whereas polarization informs us of the surface features, shape, shading, and roughness (Tyo, J. Scott 2006). The SAR data used in this work contain polarization information.

As an EM wave propagates in a given direction, the electric and magnetic fields that compose the wave are oscillating perpendicular to the direction of propagation and to each other. Polarization is the orientation of the oscillations of a wave. Because the electric and magnetic fields are instantaneously perpendicular to each other, it is sufficient to describe only one of these two components. As a matter of convention we often describe the electric field. We further decompose the electric field vector into two orthogonal components for a complete description of its

state in localized 2D space. The Cartesian x and y unit vectors are the most common basis used in this description (Graves, 1956).

A polarization state is the 2-dimensional shape that is traced out by the electric field vector in a plane perpendicular to the direction of wave propagation. If the two orthogonal components of the electric field are in phase the ratio of the amplitude of the each component is constant and the polarization state is linear. If the two orthogonal components have the same amplitude and are ninety degrees out of phase then the polarization state is circular. All other cases result in elliptical polarization. The three possible polarization states are depicted in Figure 2 (Graves, 1956).

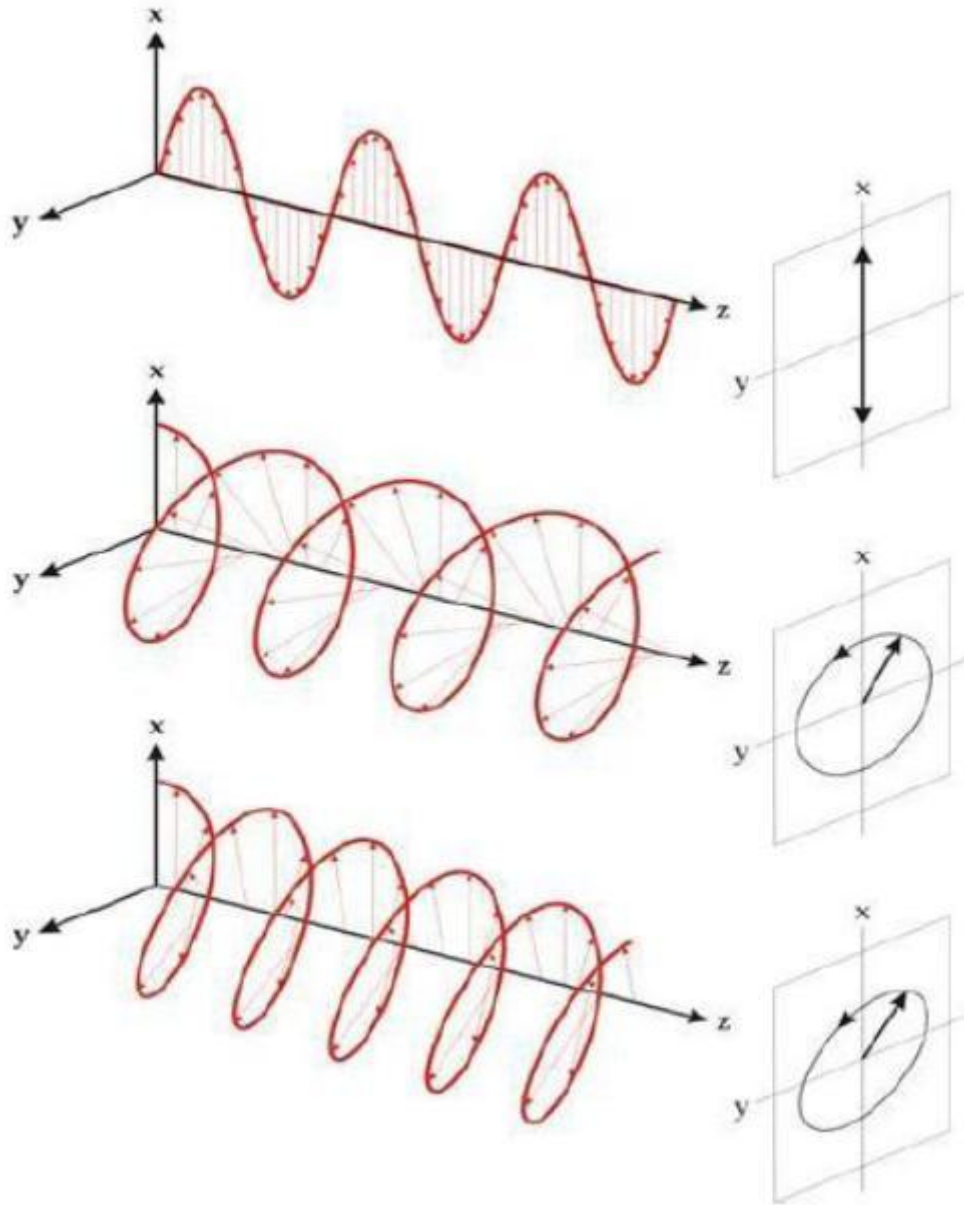


Figure 2. The three possible polarization states: linear polarization (top), circular polarization (middle), and elliptical polarization (bottom) (From Chai, 2011).

Polarization states can be described using a number of methods. One such method is the parameterization of the polarization ellipse (Ward and Smith, 1974). These parameters are the orientation angle ψ ($0 \leq \psi \leq \pi$) and the

ellipticity angle χ ($-\pi/4 < \chi \leq \pi/4$). Figure 3 shows these parameters and their relation to the polarization ellipse. The orientation angle is the angle between the X axis and the major axis of the ellipse. The ellipticity angle is the angle between the major axis and a chord connecting an intersection of the ellipse with the minor axis and the intersection of the ellipse with the major axis.

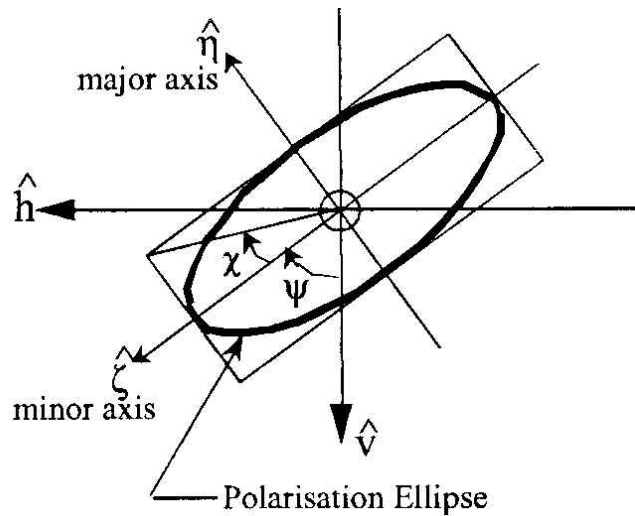


Figure 3. Polarization ellipse (From MacDonald, 1999)

B. MULTISPECTRAL IMAGING

VNIR multispectral imaging from a space-borne platform measures the intensity of the electromagnetic radiation emitted from the sun and reflected from the surface of the earth to the sensor. The wavelength bands vary from sensor to sensor. Landsat 1 was the first commercial multispectral sensor in space (Gupta, 1991). This sensor collected measurements in seven spectral bands from .475 to 1.1 micrometers usually in .1 micrometers bandwidths. Three of the bands were centered over red, green, and blue to create

true color images using the RGB color scheme and a near infrared (NIR) band was usually included. This band scheme has stood the test of time, most subsequent space borne systems and current state-of-the-art sensors such as DigitalGlobe's Worldview-2 (WV-2) sensor provide similar capabilities, albeit with smaller pixels. WV-2 data were used for the electro optical component of this study (see capabilities description below).

Remote sensing from space introduces new problems in classification of imagery. Image pixels are relatively large as a result of the Rayleigh criterion and the range of space-born sensors from the surface of the Earth. The limiting size of pixels is further reduced by atmospheric turbulence (Fried, 1966). These large pixels result in mixed pixels where multiple targets are in the same pixel and the spectral signature in the image is a combination of the two individual signatures (Smedes et al., 1975). Another problem, known as spectral variability, is the result of variation in nature of what we would consider the same target type.

C. SAR IMAGING

SAR imaging, unlike multispectral imaging, is an active imaging mode. This means that the microwave wavelength energy is generated by the sensor (the transmitting and receiving antenna can either be separate or one and the same).

A synthetic aperture radar image indicates the average returned power from the targets in the location defined by each pixel. This returned power is different for each pixel as determined by the radar cross-sections of the targets

located in each pixel. Radar cross-sections are dependent on a number of features including: target material, size of the target, relative size of the target with respect to the wavelength of the transmitted wave, incident and reflected angles, and polarization of the transmitted and received energy (Tomiyasu, 1978). I moved all citations inside sentence. Scan to make sure I did not miss any. In contrast to multispectral imaging, these image values are determined largely by the geometry and size of the scattering target.

The interactions between target and the energy are typically distinguished by the dominant scattering method involved (Tomiyasu, 1978; Cloude, 1985). There are three main methods: smooth surface, single bounce, double bounce, and volumetric scattering. Smooth surface scattering occurs when the radar energy is incident on a smooth surface relative to the wavelength of the wave. The reflected angle is approximately the incident angle and the returned energy is near zero. Rough surfaces (relative to the wavelength) scatter in all directions. Some of this energy is returned to the sensor and is known as single bounce scattering. In general, rougher surfaces have higher backscatter, again depending on SAR wavelength. Double bounces occur when two smooth surfaces, one flat on the ground and the other vertical, combine to reflect at a very high intensity. Examples of double bounce include buildings and vertical vegetation such as tree trunks. Volumetric scattering occurs when the energy interacts with a layer of randomly oriented scatterers. This is most common in vegetated areas such as forests.

Polarimetric SAR data are often recorded in a 2x2 scattering matrix indicating the intensity of the reflected radar energy with respect to a polarization basis (Cloude and Pottier, 1996). The scattering matrix can be represented using an infinite number of basis representations. A common basis is horizontal and vertical linear polarization which results in a scattering matrix similar to the one in equation 1.2

$$S = \begin{bmatrix} s_{hh} & s_{hv} \\ s_{vh} & s_{vv} \end{bmatrix} \quad \text{Equation 1.2}$$

where the first and second subscripts represent the transmitted and received polarization respectively. (Huynen, 1990) In general the cross-polarization elements s_{hv} and s_{vh} are equal (Huynen, 1990).

These data can be difficult to interpret and a number of methods called decompositions have been developed over the years to accomplish this task. In general, targets are distinguished by the dominant scattering methods discussed above. SAR decomposition methods aim to separate these scattering methods in order to distinguish targets in the image based on the level of scattering (Cloude and Pottier, 1996). See the Classification section for additional details.

D. WORLDVIEW-2 SATELLITE IMAGERY

WorldView-2 (WV-2) is a commercial multispectral satellite owned by DigitalGlobe. The satellite is capable of .5 m panchromatic and 2 m multispectral spatial resolution imagery. The WV-2 multispectral data are contained in 8 spectral bands. In addition to the more

common blue (.450-.510 micrometers), green (.510-.580 micrometers), red (.630-.690 micrometers), and near-infrared (IR) (.770-.895 micrometers), WV-2 has coastal (.400-.450 micrometers), yellow (.585-.625 micrometers), red edge (.705-.745 micrometers), and NIR 2 (.860-1.040 micrometers) bands. These additional bands provide information not normally collected by multispectral sensors (Marchisio, 2010).

The multispectral dataset used in this work was collected on April 11, 2012, using the DigitalGlobe WV-2 imaging satellite. The image scene is of the Monterey Peninsula in California. The image size is 8194 samples by 7135 lines and 8 bands at 2.25 meter spatial resolution shown in Figure 4. Only a small subset of these data (3120 samples and 2363 lines, approximately 7x5 km) were used for the combined analysis.

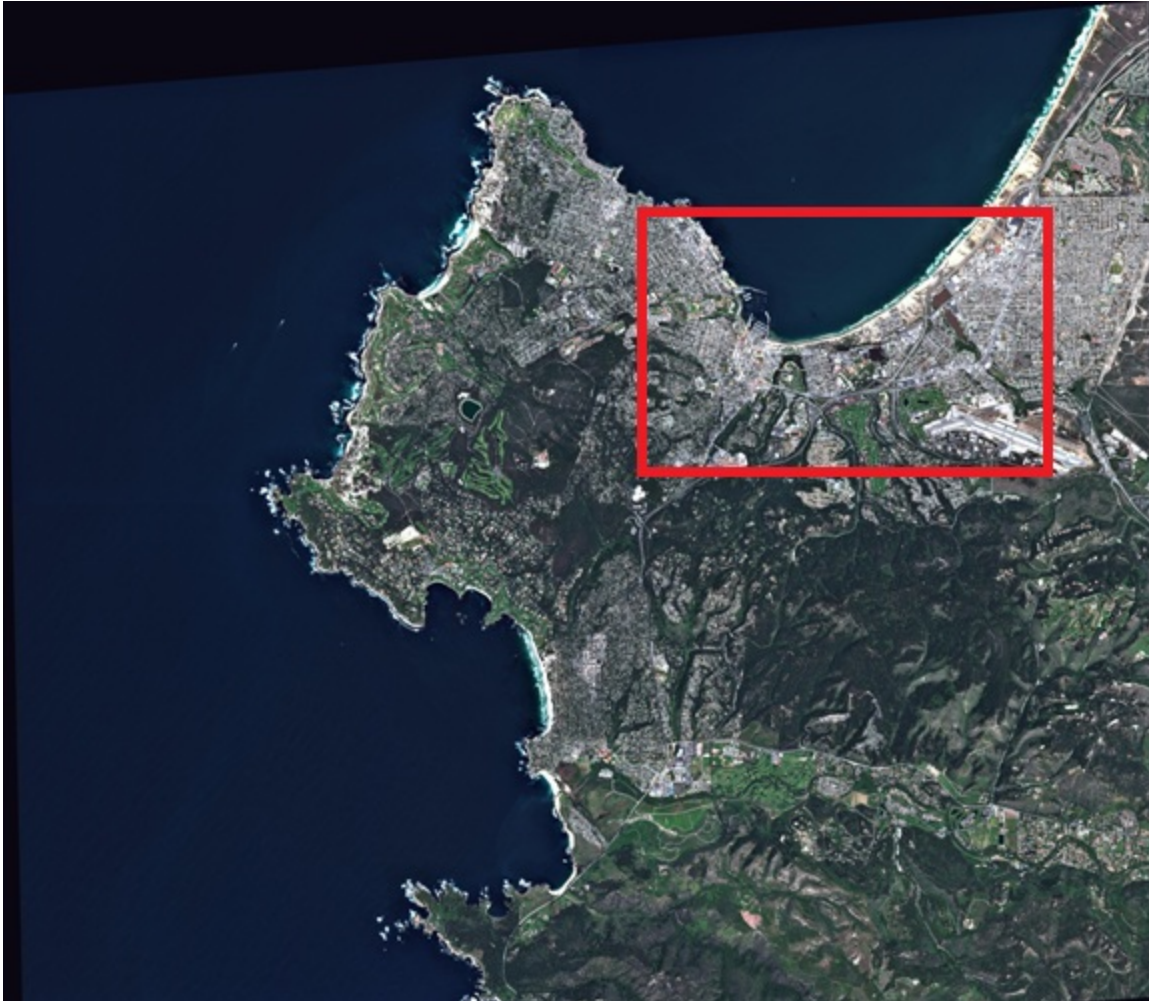


Figure 4. WV-2 Dataset. Red box outlines subset used for this study.

E. UNINHABITED AERIAL VEHICLE SYNTHETIC APERTURE RADAR (UAVSAR)

UAVSAR is a polarimetric L-band (23cm) airborne SAR sensor that is designed for repeat track collection for the purposes of interferometric measurements (Chapman, 2010). The system is capable of 2m range resolution using the optimal range bandwidth of 80 MHz. The antenna is electronically steerable which allows for more control of the antenna beam independent of air speed (Chapman, 2010).

The SAR data set used for this work was collected on November 14, 2009, using the UAVSAR L-band sensor. The scene collected includes the Monterey Peninsula along with a large swath of California to the northeast along the collection flight line (flight line ID 23025). The data used in this work have 7.2 meter azimuth resolution by 5 m range resolution. An image is shown in Figure 5. The data are distributed via the UAVSAR NASA JPL website (<http://uavsar.jpl.nasa.gov>) in compressed Stokes matrix format.

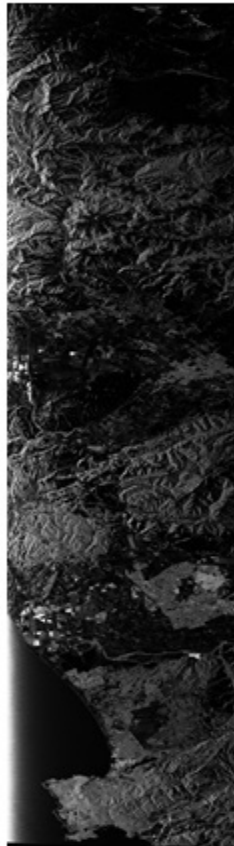


Figure 5. UAVSAR dataset

F. IMAGE CLASSIFICATION

One way in which information is extracted from image data is known as classification. Image classification is usually performed on a per pixel basis and is the process of assigning each pixel into a class. (Richards, 2005a) General land classes used for classification include urban, vegetation, and water among others.

Classification methods fall into one of two categories: supervised or unsupervised (Mohd et al., 2009). Unsupervised classification procedures separate the targets into classes without any *a priori* knowledge. An example of such a method is k-means (Hartigan and Wong, 1979). Conversely, classification can be supervised. These methods classify the image into predefined classes, usually determined using knowledge of the ground truth (Richards, 2005b). Examples of such a method include minimum distance, maximum likelihood, and Mahalanobis distance (Wacker and Landgrebe, 1971; Strahler, 1980; McLachlan, 1999). All analysis in this document was accomplished using supervised classification methods.

1. Supervised Classification Methods

Supervised classification methods are the most common classification procedures used in remote sensing applications. All supervised classification methods include the following basic steps:

1. Choose the set of classes into which the dataset will be segmented.
2. Select training data for each class.

3. Estimate the class parameters necessary for the chosen classification method using the training data.

4. Classify each pixel in the image using the selected classification algorithm (Richards, 2005b).

The minimum distance classifier has the benefit of requiring less training data than many other classifiers in order to achieve good results (Wacker and Landgrebe, 1971). The discriminant function for the minimum distance classifier is derived from the squared distance formula and has a final form of

$$x \in \omega_i \quad \text{if} \quad g_i(x) > g_j(x) \quad \text{for all} \quad j \neq i \quad \text{Equation 2.1}$$

where

$g_i(x) = 2m_i \cdot x - m_i \cdot m_i$, x is the pixel vector being classified, and ω_i is the i th class (Wacker and Landgrebe, 1972; Richards, 2005b).

The maximum likelihood classifier uses the variances of the target classes as well as the mean. The maximum likelihood decision rule classifies according to

$$x \in \omega_i \quad \text{if} \quad p(\omega_i | x) > p(\omega_j | x) \quad \text{for all} \quad j \neq i \quad \text{Equation 2.2}$$

An application of Bayes' theorem and a few simplification steps results in the following discriminant function

$$g_i(x) = -\ln |\Sigma_i^{-1}| - (x - m_i)^t \Sigma_i^{-1} (x - m_i) \quad \text{Equation 2.3}$$

where m_i and Σ_i are the mean vector and covariance matrix of the data in class ω_i (Strahler, 1980; Richards, 2005b).

Another common supervised classifier is the Mahalanobis distance classifier (McLachlan, 1999). This

method is fast while maintaining directional sensitivity similar to the maximum likelihood classifier. The discriminant function for the Mahalanobis distance classifier reduces to (McLachlan, 1999; Richards, 2005b)

$$g_i(x) = (x - m_i)' \Sigma^{-1} (x - m_i). \quad \text{Equation 2.4}$$

All three of the classifiers discussed above are used and compared in the work contained in this document. A common method for validation called the confusion matrix is the classification validation method used in this work. A confusion matrix displays information about the actual and estimated classifications (Congalton, 1991; Amrinder, 2012; Richards, 2005b)(Table 1). The numbers indicate rows and columns corresponding to the "c" classes represented in maps A and B. p_{ij} is the proportion of pixels from class i in map A classified as class j in map B. Variables p_i and $p_{.i}$ are the ratios of pixels for class i to the total number of number pixels for class i in maps A and B, respectively.

Map A categories	Map B categories				Total
	1	2	...	c	
1	p_{11}	p_{12}	...	p_{1c}	$p_{1.}$
2	p_{21}	p_{22}	...	p_{2c}	$p_{2.}$
⋮	⋮	⋮	⋮	⋮	⋮
c	p_{c1}	p_{c2}	...	p_{cc}	$p_{c.}$
Total	$p_{.1}$	$p_{.2}$...	$p_{.c}$	1

Table 1. Sample confusion matrix (From Monserud, 1992)

In the example confusion matrix below (Table 2), "a" represents the percent of pixels correctly classified from

class 1. The value represented by "b" is the percent of pixels belonging to class 1 that were incorrectly classified as class 2. The matrix element "c" corresponds to the percent of pixels belonging to class 2 that were incorrectly classified as class 1. The final element "d" is the percent of correctly classified pixels from class 2.

		Predicted	
		Class 1	Class 2
Actual	Class 1	a	b
	Class 2	c	d

Table 2. Example confusion matrix

Additional statistics are often calculated from the confusion matrix to summarize the information contained in larger confusion matrices. These include measures such as the overall accuracy, kappa coefficient, user's accuracy, and producer's accuracy (Congalton, 1991).

Overall accuracy is the ratio of correctly predicted pixels to the total number of pixels (Amrinder, 2012; Richards, 2005b). Mathematically this is computed by calculating the weighted average of the diagonal elements (Congalton, 1991).

User's accuracy is a measure of the commission error and is computed on a per class basis. The total number of correctly identified pixels in a class is divided by the total number of pixels classified as that class. This ratio represents the probability that a pixel classified as that class in the classification image correctly represents that pixel on the ground (Congalton, 1991).

Producer's accuracy is a measure of omission error and is also computed on a per class basis. The total number of correctly identified pixels for a class is divided by the number of pixels in that class in the reference data. This ratio represents the probability that a pixel from the reference data in that class will be correctly identified (Congalton, 1991).

The Kappa coefficient is a multivariate statistics calculation which indicates the proportion of correspondences between maps after chance agreement is removed from consideration (Cohen, 1960). The overall accuracy of the confusion matrix shown in Table 1 is

$$p_0 = \sum_{i=1}^c p_{ii} . \quad \text{Equation 2.5}$$

The overall proportion of chance agreement is

$$p_e = \sum_{i=1}^c p_i . p_i . \quad \text{Equation 2.6}$$

The Kappa statistic is a normalized difference between these two values defined as

$$\kappa = \frac{p_0 - p_e}{1 - p_e} . \quad \text{Equation 2.7}$$

The Kappa statistic is useful because it will be equal to one for two maps with perfect agreement and close to zero when the maps agree approximately as much as would be expected due to chance (Monserud, 1992).

Each of these summary statistics contains different information derived from the confusion matrix. These statistics can also indicate different levels of accuracy

from the same confusion matrix (Congalton, 1991). Table 3 indicates the different range of Kappa coefficients and the degree of agreement that they represent as defined by Monserud (1992). An understanding of how these various summary statistics are computed and their meaning is needed in order to determine success on a per application basis.

Lower bound	Degree of agreement	Upper bound
< 0.05	No	0.05
0.05	Very poor	0.20
0.20	Poor	0.40
0.40	Fair	0.55
0.55	Good	0.70
0.70	Very good	0.85
0.85	Excellent	0.99
0.99	Perfect	1.00

Table 3. Kappa coefficients and their degree of agreement (From Monserud, 1992)

2. Pauli Decomposition

While not strictly a classification per-se, the Pauli decomposition, applied to SAR data is a method for breaking the data down into components explaining surface scattering properties. The results can then be further classified using a variety of classification approaches. The Pauli decomposition is the most common SAR decomposition (Zhang et al., 2008). This decomposition represents the scattering matrix (Huynen, 1965) as three components representing single-bounce, double-bounce, and volumetric scattering mechanisms. In comparison to other coherent decomposition methods, the Pauli decomposition is excellent for exposing

natural targets, but not ideal for highlighting man-made targets (Zhang et al., 2008).

The scattering matrix $[S]$ can be written as:

$$[S] = \begin{bmatrix} s_{hh} & s_{hv} \\ s_{vh} & s_{vv} \end{bmatrix} = \alpha \begin{bmatrix} 1 & 0 \\ 0 & 1 \end{bmatrix} + \beta \begin{bmatrix} 1 & 0 \\ 0 & -1 \end{bmatrix} + \gamma \begin{bmatrix} 0 & 1 \\ 1 & 0 \end{bmatrix} \quad \text{Equation 2.8}$$

where $\alpha = (s_{hh} + s_{vv})/\sqrt{2}$, $\beta = (s_{hh} - s_{vv})/\sqrt{2}$, and $\gamma = \sqrt{2}s_{hv}$.

The Pauli decomposition's dimensionality of three makes it simple to represent visually using the RGB color scheme. Often the α , β , and γ components are represented as blue, red, and green respectively resulting in an image similar to the example shown in Figure 6.



Figure 6. Example Pauli decomposition image of the San Francisco, California, area (From Lee & Pottier, 2009)

This image of San Francisco, CA, shows the water as having relatively high single bounce returns, the urban areas having mixed returns but significantly higher double bounce than other areas, and the vegetated areas as having a high volumetric scattering return.

3. Data Fusion

Data fusion is the combination of data from multiple sources motivated by the possibility of generating a different interpretation of the scene than is obtainable by a single source (Sohlberg et al., 1994).

The type of data fusion being performed is categorized based on at which step during processing the fusion occurs. Pixel level fusion occurs when the fusion is performed between the base images. Feature level fusion occurs when features are extracted from the images before fusion occurs, e.g., using segmentation procedures. Decision level fusion is a method that uses information extracted from each image along with decision rules to resolve differences between the features (Pohl & Genderen, 2010).

In 1990, SPOT panchromatic image data were fused with SPOT multispectral data for visual interpretation using an intensity-hue-saturation (IHS) transform (Haydn et al., 1982; Carper et al., 1990). The resulting image had higher resolution but correlation analysis indicated that care must be used in the analysis of the resulting spectral characteristics. Pixel level fusion is not limited to fusion of remotely sensed images. In 1989 radar imagery was combined with geophysical data into an IHS image that summarized the information contained in both (Harris and Murray, 1999). Feature level fusion has been shown to be of

use in creating land cover maps for nuclear incident response (Sah et al., 2012). In this case classification maps were created from multiple sensors and then merged to create a final classification map of increased accuracy. In 1995 decision level fusion was performed using neural networks to perform unsupervised classification with good results (Baraldi and Parmiggiani, 1995). Advantages of this approach include not needing a priori knowledge of the scene and fast computation times. Because no a priori knowledge of the scene is used, however, there is no "correct" classification using this method since classification is unsupervised (Baraldi and Parmiggiani, 1995).

Data fusion between different sensors often requires working with different spatial, spectral, or temporal characteristics. It has been shown that the use of data of different spatial resolutions can be beneficial when applied to forest mapping (Kempeneers et al., 2011). The effects of the differing acquisition dates of the datasets were not however considered for the purposes of this research.

THIS PAGE INTENTIONALLY LEFT BLANK

III. METHODS

The following sections outline the work that was performed in order to construct the fused dataset and also the classification and post-processing evaluation steps that were taken to validate the work.

A. FLAASH ATMOSPHERIC CORRECTION

Atmospheric correction algorithms are used on spectral datasets to correct or compensate for the effects of atmospheric propagation in remotely sensed data. Fast Line-of-sight Atmospheric Analysis of Spectral Hypercubes (FLAASH) is an atmospheric correction algorithm based on the MODerate resolution atmospheric TRANsmission (MODTRAN4) atmospheric transfer model developed by the Air Force Phillips Laboratory, Hanscom AFB and Spectral Sciences, Inc (SSI) (Cooley et al., 2002).

The goals of the FLAASH algorithm are to provide accurate atmospheric properties in order to calculate a correction matrix to convert the radiance value recorded at the detector to surface reflectance (Cooley et al., 2002). In order to do this the FLAASH uses the equation below to calculate the pixel reflectance.

$$L^* = \frac{A\rho}{1-\rho_e S} + \frac{B\rho_e}{1-\rho_e S} + L_a^* \quad \text{Equation 3.1}$$

where L^* is the radiance at a sensor pixel, ρ is the pixel surface reflectance, ρ_e is the surface reflectance averaged over a pixel and the surrounding region, S is the spherical albedo of the atmosphere, L_a^* is the radiance backscattered

by the atmosphere, and A and B are coefficients determined by the atmospheric and geometric conditions of the collection and are calculated using the MODTRAN atmospheric model. The second term in the equation makes FLAASH unique from other correction algorithms in that it accounts for adjacency effects (Matthew et al., 2002).

The WorldView-2 data were corrected using the FLAASH algorithm. Use of the FLAASH algorithm requires knowledge of the geolocation of the image, acquisition date/time, pixel size, sensor altitude, ground elevation, and sensor characteristics. FLAASH was chosen because it has been shown to produce comparable results to competing atmospheric correction algorithms while accounting for adjacency effects and non-nadir viewing sensor angles (Kruse, F. A., 2004).

B. REGISTRATION

The superposition process requires that the co-registration between two images have very little error for the data fusion to be meaningful. To make this possible, relatively small chips were taken from the original datasets. The WV-2 dataset is 8,194 samples and 7,135 lines at 2.25m resolution. A chip of 3,120 samples and 2,363 lines was taken from the downtown Monterey area. This area was selected because it contains numerous distinct features to use as tie points for the registration process and also contained numerous ground cover classes for the classification step.

The UAVSAR dataset are 3,300 samples by 14,664 lines. These data were chipped down to 2,400 samples by 2,265 lines at 7 by 5 meter resolution over an area containing the entirety of the WV-2 data chip.

Manual selection of ground control points (GCPs) was performed using geographic features, road intersections, and building corners. In total 74 GCPs were selected. Using the WV-2 data as the base image and warping the UAVSAR data to this dataset, the two images were co-registered using the triangulation method with nearest neighbor resampling. After warping the UAVSAR data, a final data chip was selected to correspond in both size and space with the WV-2 resulting in a 3120 samples by 2363 lines at 2.25 meter resolution dataset. The error for first order polynomial registration using the selected GCPs (a worst case estimate for triangulation error) was 5.34 pixels. The final data sets are shown in Figure 7.

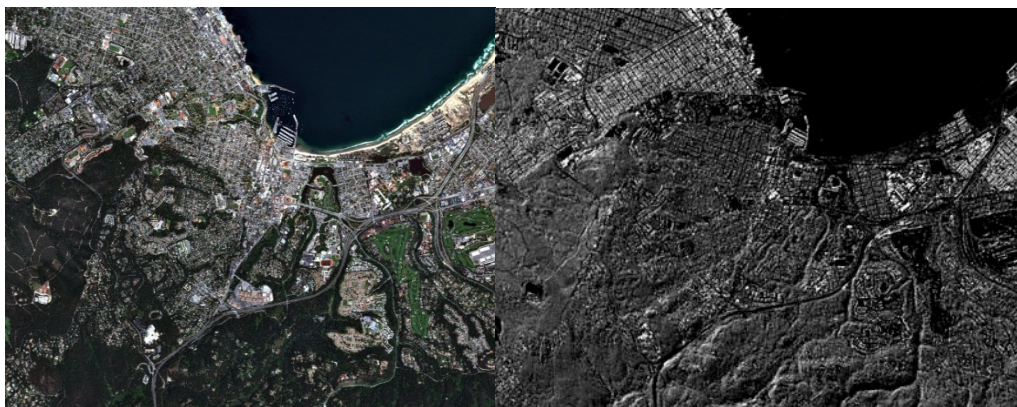


Figure 7. Final registered datasets. Left: WV-2, Right: UAVSAR

C. WV-2 CLASSIFICATION

Classification was done on the WV-2 dataset using the minimum distance, maximum likelihood, and Mahalanobis distance decision rules. Eight regions of interest (ROI) were selected using a true color composite and the ground truth was verified in person Figure 8 shows a true color image of the scene with the ROIs overlaid. Each site was visited individually to verify via inspection that the ROIs represent their class names. The red ROI is a selection of urban areas between roads. This ROI has a lot of spectral variability as expected. The blue ROI is an arbitrary selection of the ocean in the image. This region has relatively low spectral variability. The green region is a selection of "dense" trees. In this case dense means an area of trees that is dense enough to prevent visibility of the ground from above at 2.25 meter resolution. The yellow region is a selection from a couple of the golf courses in the area. In an effort to limit the spectral variability of this region, only fairway grass was selected. The cyan region is a selection of some of the baseball outfields in the image. The magenta region is a selection of the sandy beaches. These beaches can have low to high spectral variability depending on the tides; the separation in acquisition dates between data sets may affect the results more significantly in this region. The maroon region is a selection of the local highways. At this resolution vehicles are resolved and do increase the spectral variability for this region. The sea green region is a selection of "less dense" trees. In this region the ground is clearly visible in between the trees.

Figure 8 is an image of the Monterey data set with the selected ROIs overlaid. Figure 9 illustrates the high spectral variability of the urban region. On the left is a plot of the min/mean/max spectra from the urban region. The black curve is the mean spectrum from the ROI. The green curves are spectra that are one standard deviation from the mean. The red curves are the upper and lower envelope spectra from the urban region. The plot on the right is randomly selected spectra from the urban region.

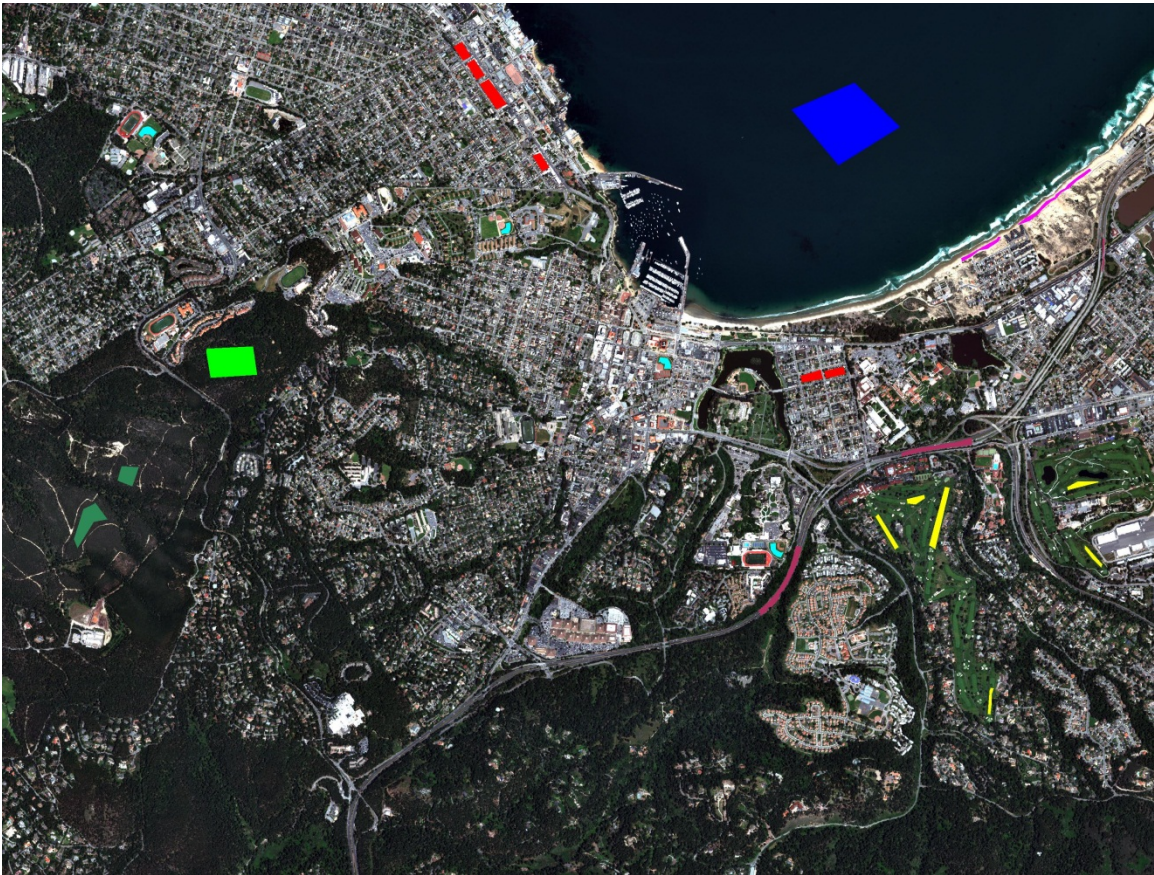


Figure 8. WV-2 true color image of the Monterey subset with ROIs overlaid

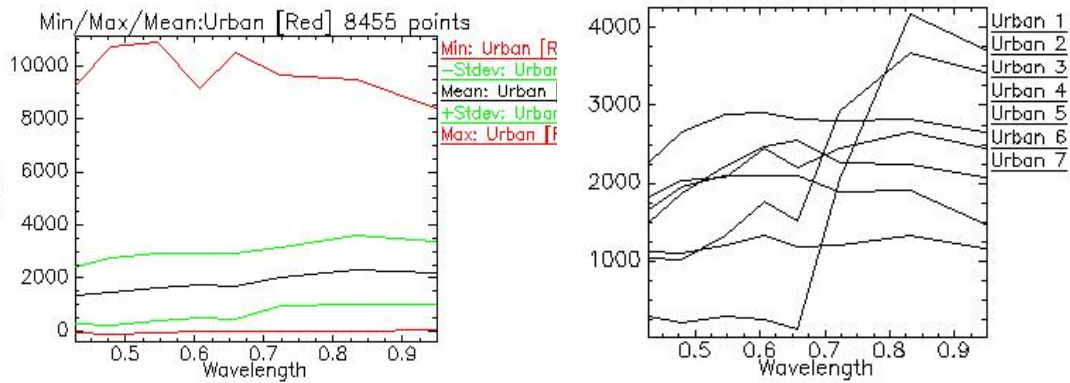


Figure 9. Urban ROI mean/min/max spectra (left) and sample pixel spectra (right)

Classification results for all classification approaches applied were validated using the confusion matrix method with ground truth provided by ROI selections for the same classes but in different locations in the scene as shown in Figure 10. The ground truth was verified locally.



Figure 10. WV-2 data with reference ROIs overlaid

D. PAULI DECOMPOSITION COMPUTATION AND FUSION

The Pauli decomposition for the UAVSAR data was computed using the the formulas described in Chapter II of this work. The RGB image of the Pauli decomposition, where α is blue, β is red, and γ is green, is shown in Figure 11.



Figure 11. Pauli decomposition image

The image shows that the SAR scene contains mostly volumetric scattering (green). There are almost no areas of well-defined single (blue) or double bounce (red) scattering. The majority of areas that are not volumetric scattering are a combination of single and double bounce scattering, which results in the pink regions. The dependence of SAR data on the angle between the flight line and target geometry is apparent in this image. Urban sections with buildings and streets aligned along the upper left to lower right diagonal of the image resulted in high

single and double bounce values. Those neighborhoods aligned in other directions returned very low single and double bounce values.

The multispectral classification methods were run on the three band Pauli decomposition. The overall accuracy of this classification was very low and not very meaningful. A short analysis of one of the three classification methods can be found in the results section while the classification images and confusion matrices for the other two methods can be found in Appendix A. The three band image that resulted was concatenated with the eight band WV-2 data which resulted in an image with 11 dimensions per pixel. The fused 11 dimension dataset was classified using the same three algorithms and reference data as the WV-2 dataset. The resulting classification images were used to compute confusion matrices for comparison with the WV-2 classifications.

THIS PAGE INTENTIONALLY LEFT BLANK

IV. RESULTS

The WV-2 classification results are shown in Figures 13-19. Figure 12 is the classification map legend for reference to be used with all classification images.

Figure 13 is the multispectral imagery (MSI) Mahalanobis distance classification image. On inspection, the Mahalanobis distance classification image looks positive. The water line at the beach is very distinct. The less dense trees region on the left side of the image is fairly well separated from the dense trees. Baseball fields, and golf courses are generally well classified. However, specific problem areas exist in this image. The water classification shows errors of commission on four football fields throughout the image. The urban region is also heavily under-classified. Also, many roads are incorrectly classified as urban. The beach region does not appear to have many errors of omission, however, there are many urban regions incorrectly classified as beach.









	Urban {Red}	8455 points
	Water {Blue}	33939 points
	Dense Trees {Green}	9982 points
	Golf Course {Yellow}	6672 points
	Baseball Outfield {Cyan}	2600 points
	Beach {Magenta}	2800 points
	Road/Highway {Maroon}	5820 points
	Less Dense Trees {Sea Green}	6324 points

Figure 12. Classification image ROI key

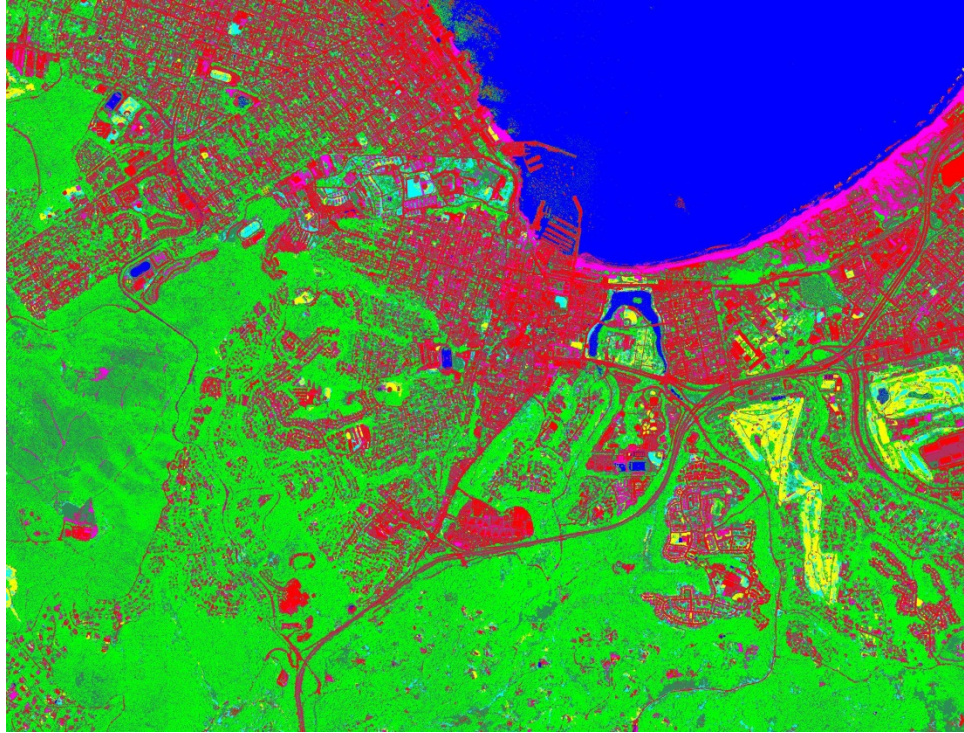


Figure 13. MSI Mahalanobis distance classification

Figure 14 is the MSI maximum likelihood classification image. Despite having higher overall accuracy based on the ground truth ROIs, the maximum likelihood classification image appears to have many more misclassifications. The urban class has a number of false positives throughout the image. Most obvious is the misclassification of the ocean near the beach as urban and the horseshoe shaped body of water in the middle of the image. Once again, golf courses, baseball fields, and roads are classified well. The less dense trees are well classified near the training data but not elsewhere in the image.



Figure 14. MSI maximum likelihood classification

Figure 15 is the MSI minimum distance classification image. It is notable that the "rough" around the fairways in the golf courses were classified as baseball field which should be considered a correct classification. However, this image appears to have the most errors throughout the image. There are a lot of areas classified as water throughout urban areas, and in one case a track and field track is classified as water. The beach region is also over classified in the urban areas. Roads are under-classified, often as urban.

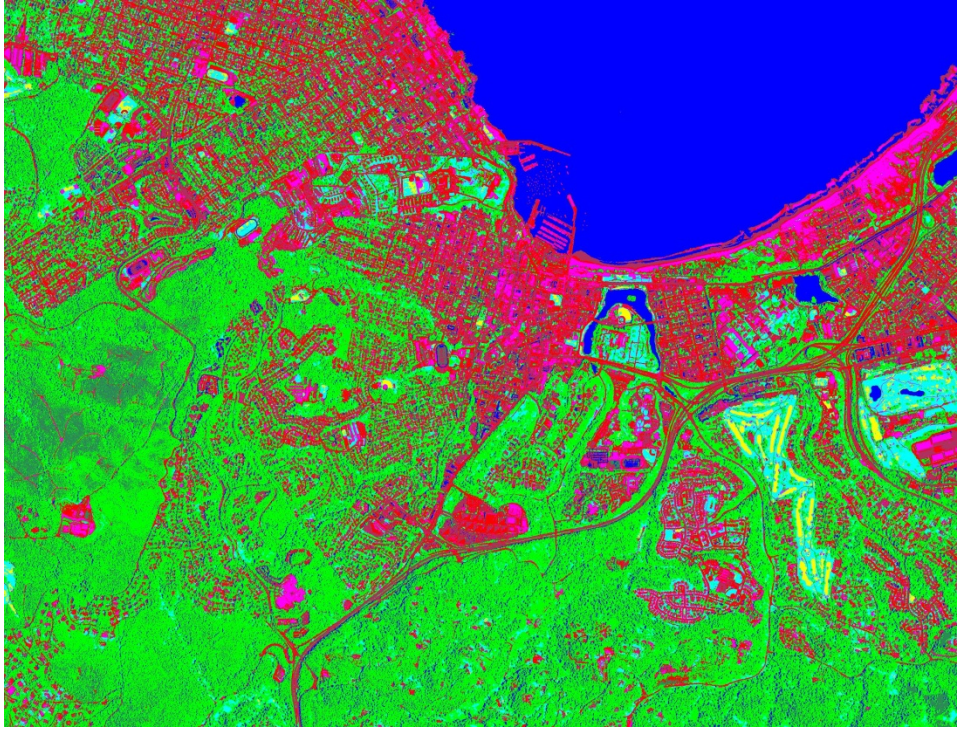


Figure 15. MSI minimum distance classification

The confusion matrices from the three classification methods are shown in the tables below in percent accuracy form. For readability, class names were changed to numbers corresponding to Table 4.

Class name	Class number
Urban	1
Water	2
Dense trees	3
Golf course	4
Beach	5
Less dense trees	6
Roads	7
Baseball field	8

Table 4. Confusion matrix legend

Table 5 is the confusion matrix for the Mahalanobis distance classification results. Mahalanobis distance classification had the median accuracy and kappa coefficient of 71.73% and .6559 respectively. The degree of agreement for this classification is "good," according to Table 3. Statistics to note within the table include: 100% producer accuracy for the beach region and near 100% producer and user accuracies for the water region. The producer accuracy was especially low for the urban as expected because of the number of omissions apparent in the image. The user accuracy was low for the road region (27%) due to a high percentage of the urban region being classified as road.

Predicted Class	Reference Class								Total
	1	2	3	4	5	6	7	8	
1	41.77	0.01	0.97	0	0	0	52.14	0.53	11.04
2	1.67	99.98	0.58	0	0	0	1.23	0.05	33.19
3	5.48	0	68.85	0	0	0.07	0.18	41.74	14.24
4	8.4	0	0	100	0	0	1.54	0	8.21
5	0.17	0	0.03	0	46.54	20.49	0	2.45	4.86
6	2.32	0	1.01	0	53.46	78.89	0.13	4.29	9.69
7	29	0.01	0.07	0	0	0.07	41.92	0.1	7.86
8	11.19	0.01	28.49	0	0	0.47	2.86	50.85	10.91
Total	100	100	100	100	100	100	100	100	100

Table 5. MSI Mahalanobis distance confusion matrix

Class	Prod. acc.	User acc.
1	41.77	74.41
2	99.98	98.57
3	68.85	65.32
4	100	78.92
5	46.54	68.55
6	78.89	50.25
7	41.92	27.04
8	50.85	42.94

Table 6. MSI Mahalanobis distance user/prod. acc.

Table 7 is the confusion matrix for maximum likelihood. Maximum likelihood had the highest overall accuracy and kappa coefficient of 83.73% and .8014 respectively which indicates a "very good" degree of agreement. The water, dense trees, and beach regions had the highest producer accuracies. The beach and water regions had the highest user accuracies. The road region once again had low user accuracy (38%) once again mostly because of misclassification between road and urban. The most significant change in the maximum likelihood results is the increase in baseball field user accuracy from 43% to 85%. The number of commissions in baseball field classification is likely the result of a drop in overall classification percentage from 10.9% to 4.62%.

Predicted Class	Reference Class								Total
	1	2	3	4	5	6	7	8	
1	62.3	0.09	0.86	0.06	0.79	2.13	18.85	0.82	13.62
2	0	99.74	0	0	0	0	0	0	32.64
3	2.71	0	94.07	0	0	0.18	0.09	47.6	17.64
4	0.36	0	0.28	83.1	0	5.13	0	8.52	7.16
5	0.11	0	0	0	99.21	0	0	0	6.45
6	0.02	0	0	16.83	0	92.56	0	0	6.92
7	34	0.17	0.36	0	0	0	81.07	0.41	10.94
8	0.49	0	4.43	0	0	0	0	42.64	4.62
Total	100	100	100	100	100	100	100	100	100

Table 7. MSI maximum likelihood distance confusion matrix.

Class	Prod. acc.	User acc.
1	62.3	89.99
2	99.74	100
3	94.07	72.02
4	83.1	83.08
5	99.21	99.65
6	92.56	82.53
7	81.07	37.54
8	42.64	84.99

Table 8. MSI maximum likelihood user/prod. acc.

Table 9 is the confusion matrix for the minimum distance classification results. The minimum distance classification rule had the lowest overall accuracy and kappa coefficient of 66.93% and 0.5971 respectively. This Kappa statistic indicates a "good" degree of agreement. The urban and roads classes had very low individual class accuracies which contributed heavily to lower overall accuracy for minimum distance. The urban and less dense trees regions had notably low producer accuracies of 27% and 34% respectively. This is due to the high number of commission errors from several other classes in these two

areas. The user accuracies ranged from 23% (road region) to 94% (water region). The low user accuracy for the urban class is correlated with the low producer accuracies for regions with commission errors in urban regions.

Predicted Class	Reference Class								Total
	1	2	3	4	5	6	7	8	
1	26.69	0	0.07	0	0.14	0.11	55.97	0.05	8.12
2	4.71	100	8.99	0	0	0	0.04	0.46	34.91
3	6.27	0	67.05	0	0	0.07	0.4	59.13	15.76
4	0.01	0	0	62.22	0	39.68	0	0	6.9
5	21.29	0	0	0	99.86	0.07	1.32	0	10.74
6	2.32	0	0.35	37.78	0	60.07	0.04	6.27	7.5
7	35.94	0	0	0	0	0	41.83	0.02	9.19
8	2.77	0	23.55	0	0	0	0.4	34.07	6.88
Total	100	100	100	100	100	100	100	100	100

Table 9. MSI minimum distance confusion matrix

Class	Prod. acc.	User acc.
1	26.69	64.71
2	100	93.74
3	67.05	57.45
4	62.22	64.49
5	99.86	60.31
6	60.07	49.46
7	41.83	23.05
8	34.07	45.59

Table 10. MSI minimum distance user/prod. acc.

Figure 16 is the maximum likelihood classification for the SAR Pauli Decomposition image. Inspection of this image indicates a low overall accuracy. There are almost no urban or road classifications at all. Beach is incorrectly classified throughout the image as roads and urban. The

golf courses and baseball fields are classified as water. Also a large portion of the image is incorrectly classified as golf courses.

The corresponding confusion matrix is displayed below in Table 11. The overall accuracy and Kappa coefficient were 48.94% and .3666 respectively. The only class with high accuracy is the water class; however, even this number is skewed by the sampling of the ground truth ROI method. The image indicates lower accuracy than 98.87%. The golf course, baseball field, and roads regions had producer and user accuracies below 6%. This indicates that almost every pixel classified as one of these classes was incorrect. These results indicate that general multispectral classification techniques do not work well for this site on the SAR data alone. The remaining classification images and confusion matrices for the SAR classifications can be found in Appendix A.

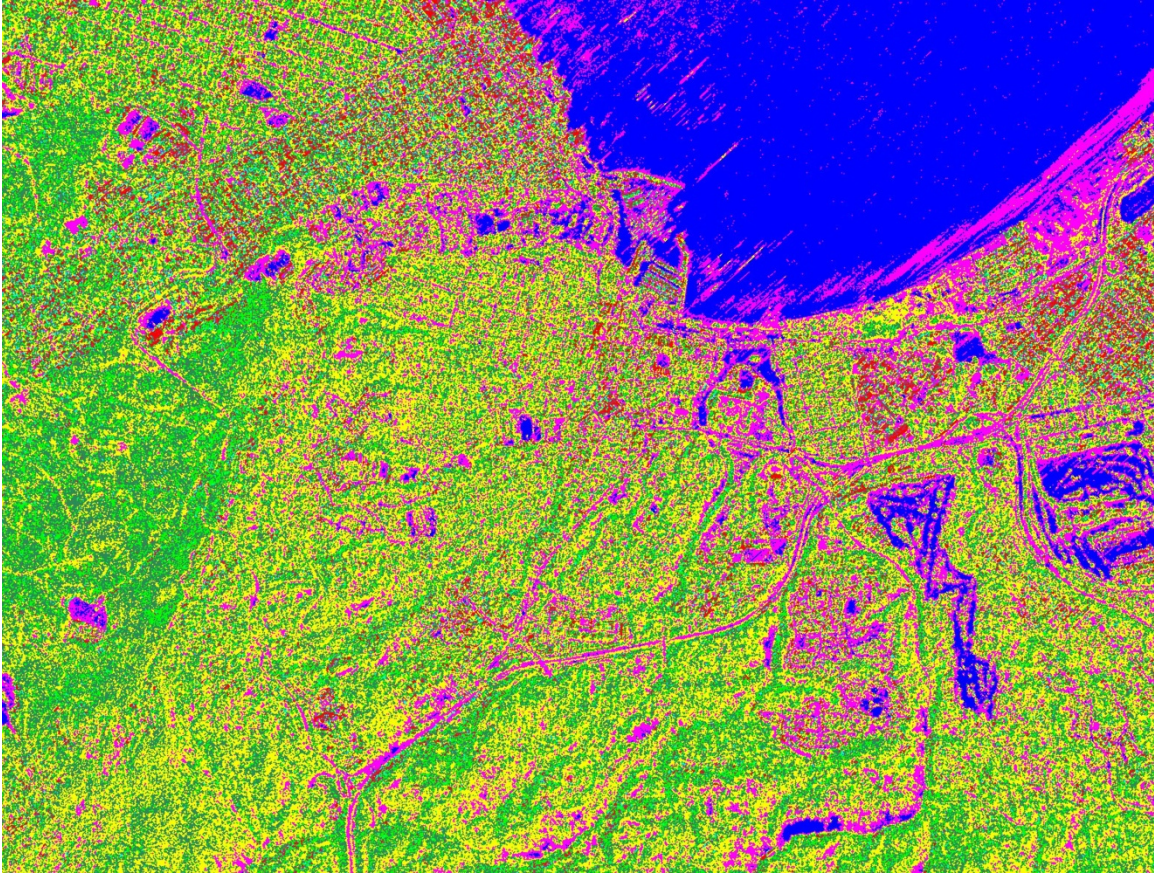


Figure 16. SAR maximum likelihood classification image.

Predicted Class	Reference Class								Total
	1	2	3	4	5	6	7	8	
1	24.04	0	0.79	0	0	0.4	3.04	0	5.02
2	0.02	98.87	0.02	65.02	42.5	50.7	13.03	0.24	43.58
3	6.37	0	32.92	0.28	0	0.76	2.77	5.04	6.37
4	21.92	0	22.23	5.17	0	3.43	14.53	36.08	11.96
5	10.15	1.13	0.81	27.46	57.5	41.92	59	22.37	15.81
6	9.31	0	0.91	0	0	0.36	1.67	0.77	2.13
7	12.45	0	3.82	0.44	0	0.98	1.06	0.34	3.14
8	15.75	0	38.5	1.62	0	1.45	4.89	35.16	11.99
Total	100	100	100	100	100	100	100	100	100

Table 11. SAR maximum likelihood confusion matrix

Class	Prod. acc.	User acc.
1	24.04	94.31
2	98.87	74.23
3	32.92	69.78
4	5.17	3.1
5	57.5	23.58
6	0.36	1.05
7	1.06	1.7
8	35.16	27.01

Table 12. SAR maximum likelihood user/prod. acc.

After pixel level fusion was performed, the same classification algorithms were run on the combined data set. The classification images that resulted are shown in figures 17-19.

Figure 17 is the Mahalanobis distance classification image of the combined dataset. This image has an overall accuracy of 74.34% and Kappa coefficient of .6884. This is an increase of almost 3% in accuracy and a "good" degree of agreement.

Inspection of the Mahalanobis distance classification image for the combined dataset reveals the most prominent difference between the MSI+SAR and the MSI classification to be an increased number of road classifications in urban areas with roads aligned in the left to right direction. Also, there is an increase in urban classifications in urban regions where the roads are aligned along the diagonal from the upper left to the lower right of the image. This is due to the contributions made by the SAR data in areas with higher single and double bounce intensities. There is also a small increase in urban classifications in some of the dense trees regions.



Figure 17. MSI+SAR Mahalanobis distance classification image.

Figure 18 is the maximum likelihood classification image that resulted from the combined MSI+SAR dataset. There was a 3% decrease in overall accuracy (down to 80.49% from 83.73%) and the Kappa coefficient dropped to .7627. Despite the decrease in the Kappa coefficient the degree of agreement remains "very good."

Despite this reduction in accuracy, inspection of the image indicates some areas of improved classification in this image. The heavy over classification of the urban region that resulted in the initial maximum likelihood image is reduced. For example, the region of the ocean that

has been classified as urban is approximately half the width as it was. Many dense trees areas that were incorrectly classified as urban are now, at least in part, correctly classified. Also, areas of the beach that were incorrectly classified as urban are now more properly classified as a mix of beach and trees (both sparse and dense). Inland bodies of water are still not correctly classified. Also there is an increase in the number of dense tree classifications along the water line. These classifications are incorrect. The impact of the line of flight of the SAR data is less apparent in this example than in the Mahalanobis distance classification.

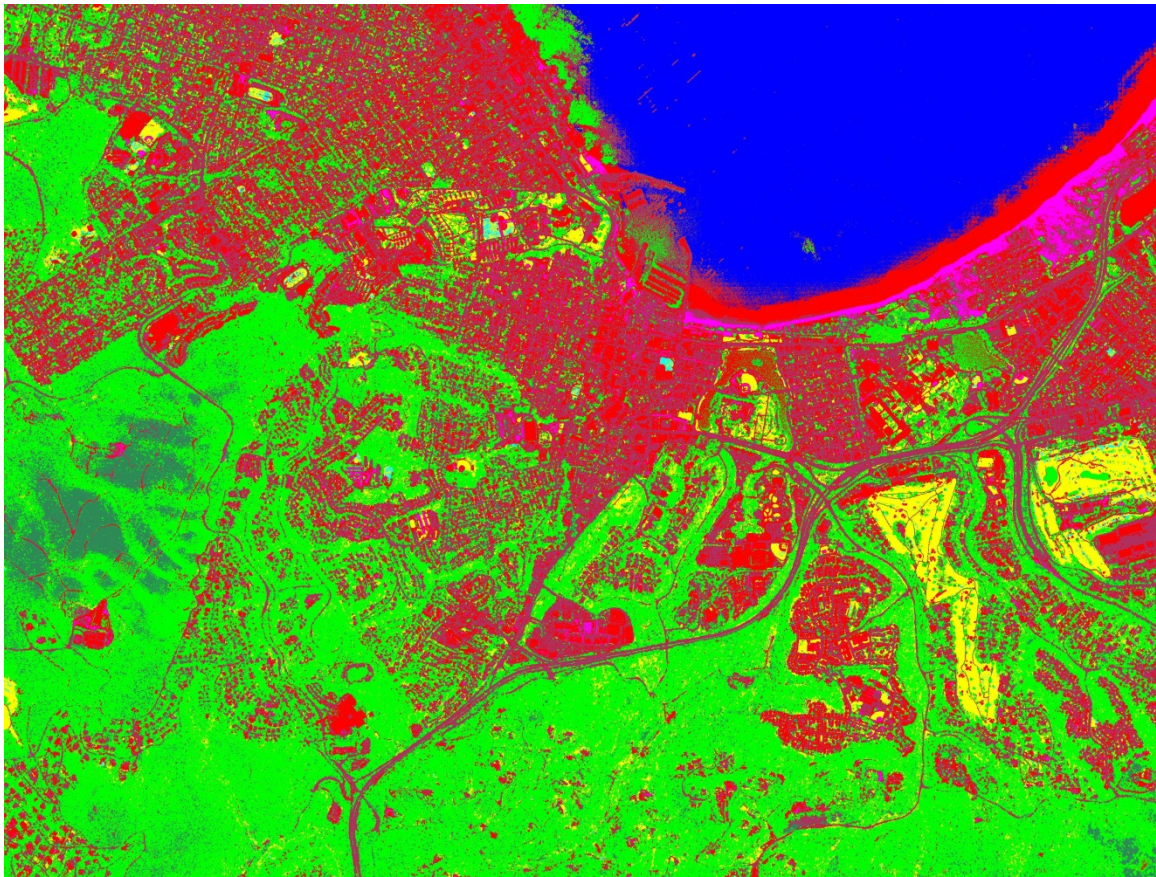


Figure 18. MSI+SAR maximum likelihood classification image.

Figure 19 is the minimum distance classification image from the combined MSI+SAR dataset. These results are identical to the MSI results. The addition of the SAR data did not increase the separation of the class clusters enough to change any classifications.

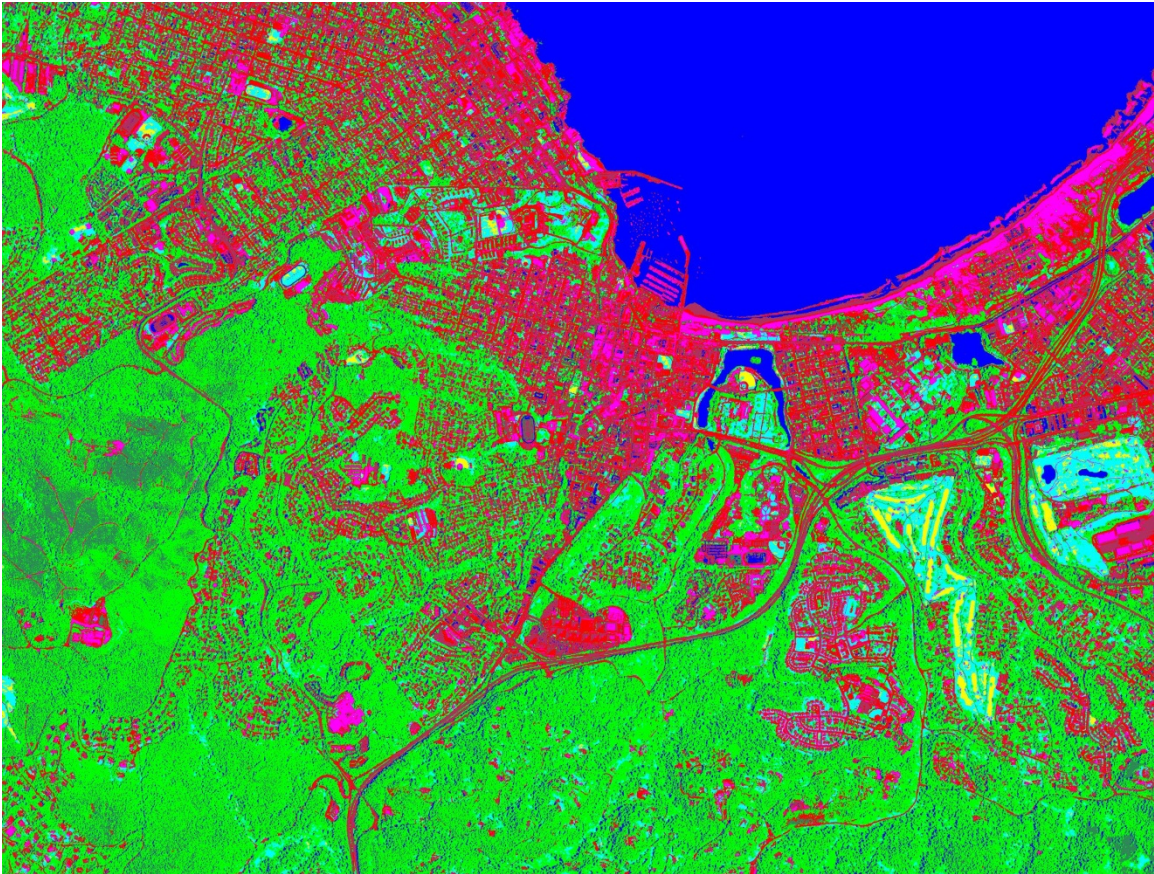


Figure 19. MSI+SAR minimum distance classification image.

The corresponding confusion matrices from the fused dataset classification images are in tables 13,15, and 17. Table 13 is the Mahalanobis distance confusion matrix for the combined dataset. Overall accuracy improved by less than 3% and the kappa coefficient improved by .03. Neither of these are significant improvements. However, certain

classes did show significant improvement in producer or user accuracy. The road class showed an improvement of 30% in producer accuracy and almost 20% in user accuracy. This is due to the increase in road classifications in urban areas in general. Roads were not over-classified in the area of the reference data because the reference data is in an area with high single and double bounce intensities. This resulted in higher urban classification accuracy. The urban class had a significant increase in user accuracy of 17%.

Predicted Class	Reference Class								Total
	1	2	3	4	5	6	7	8	
1	44.76	0	0.3	0	0	0.22	15.15	0.02	9.63
2	1.7	99.99	0.64	0	0	0	1.45	0.05	33.22
3	5.2	0	69.76	0	0	0.07	0.18	41.28	14.26
4	0.19	0	0.03	46.66	0	20.46	0	2.47	4.87
5	6.26	0	0	0	100	0	2.07	0	7.82
6	2.26	0	1.09	53.34	0	78.71	0.13	4.26	9.67
7	28.72	0.01	0.05	0	0	0.07	77.5	0.02	9.59
8	10.91	0.01	28.13	0	0	0.47	3.52	51.89	10.94
Total	100	100	100	100	100	100	100	100	100

Table 13. MSI+SAR Mahalanobis distance confusion matrix

Class	Prod. acc.	User acc.
1	44.76	91.45
2	99.99	98.5
3	69.76	66.06
4	46.66	68.54
5	100	82.91
6	78.71	50.27
7	77.5	40.93
8	51.89	43.72

Table 14. MSI+SAR Mahalanobis distance user/prod. acc.

Table 15 is the maximum likelihood confusion matrix for the combined dataset. The overall statistics for maximum likelihood also showed a marginal regression of 3% in overall accuracy and .04 in the kappa statistic. Despite this, there were notable increases in producer accuracy for the golf course and road regions of 15% and 11% respectively. The producer accuracy for the baseball field region decreased by almost 60%, and the user accuracy for the golf course region decreased by 30%. This is due largely to a high correlation between the omission error pixels for golf course and the commission error pixels for baseball field.

Predicted Class	Reference Class								Total
	1	2	3	4	5	6	7	8	
1	56.47	0.01	0.59	0.09	0.1	1.26	6.08	0.07	11.6
2	0	99.93	0	0	0	0	0	0	32.7
3	3.88	0	90.85	0	0	0.18	0.26	34.36	16.22
4	0.69	0	0.76	98.66	0	65.23	0	20.36	13.2
5	0.58	0	0	0	99.9	0	1.19	0	6.65
6	0.06	0	0	1.25	0	33.21	0	0	2.15
7	37.45	0.06	0.61	0	0	0.11	92.43	0.27	12.19
8	0.87	0	7.19	0	0	0	0.04	44.94	5.29
Total	100	100	100	100	100	100	100	100	100

Table 15. MSI+SAR maximum likelihood confusion matrix

Class	Prod. acc.	User acc.
1	56.47	95.79
2	99.93	100
3	90.85	75.63
4	98.66	53.48
5	99.9	97.38
6	33.21	95.33
7	92.43	38.43
8	44.94	78.35

Table 16. MSI+SAR maximum likelihood user/prod. acc.

Table 17 is the minimum distance confusion matrix for the combined dataset. There was no change in the results for the minimum distance classification between the WV-2 dataset and the combined dataset.

Predicted Class	Reference Class								Total
	1	2	3	4	5	6	7	8	
1	26.69	0	0.07	0	0.14	0.11	55.97	0.05	8.12
2	4.71	100	8.99	0	0	0	0.04	0.46	34.91
3	6.27	0	67.05	0	0	0.07	0.4	59.13	15.76
4	0.01	0	0	62.22	0	39.68	0	0	6.9
5	21.29	0	0	0	99.86	0.07	1.32	0	10.74
6	2.32	0	0.35	37.78	0	60.07	0.04	6.27	7.5
7	35.94	0	0	0	0	0	41.83	0.02	9.19
8	2.77	0	23.55	0	0	0	0.4	34.07	6.88
Total	100	100	100	100	100	100	100	100	100

Table 17. MSI+SAR minimum distance confusion matrix

Class	Prod. acc.	User acc.
1	26.69	64.71
2	100	93.74
3	67.05	57.45
4	62.22	64.49
5	99.86	60.31
6	60.07	49.46
7	41.83	23.05
8	34.07	45.59

Table 18. MSI+SAR minimum distance user/prod. acc.

Table 19 is a summary of the classification results' overall accuracies and Kappa coefficients before and after fusion. The overall accuracies and Kappa coefficients did not change much after fusion, however, inspection of the classification images indicated improvement in the classifications not shown in the confusion matrices. These improvements were particularly evident for the urban regions distinguished in the Pauli decomposition image. The negligible and sometimes negative change in accuracy despite the apparent improvement in accuracy is likely due to the limited scope of the method of ROI selection used to quantify the error. Using ground truth ROIs instead of a ground truth image approximates the error using a sample.

		MSI Classification	MSI+SAR Classification
Mahalanobis distance	Accuracy	71.73%	74.34%
	Kappa coefficient	0.6559	0.6884
Maximum likelihood	Accuracy	83.73%	80.49%
	Kappa coefficient	0.8014	0.7627
Minimum distance	Accuracy	66.92%	66.92%
	Kappa coefficient	0.5971	0.5971

Table 19. Results summary table.

V. CONCLUSIONS

Data from the UAVSAR and WorldView-2 sensors of Monterey, CA were successfully fused. VNIR multispectral data were analyzed. A common SAR decomposition, the Pauli decomposition was performed and inspected. The SAR Pauli decomposition and the multispectral reflectance data were fused at the pixel level, then analyzed using multispectral classification techniques. The results were compared to the multispectral classifications using the SAR decomposition results for a basis of interpreting the changes. The resulting confusion matrices showed little to no improvement in accuracy based on the samples used for reference ROIs, however, visual inspection of the classification images revealed a subjective increase in overall accuracy in two of the maps (Mahalanobis distance and maximum likelihood). The minimum distance classifier experienced essentially no change in results from the addition of the SAR information.

The most noticeable increases in classification accuracy occurred in spatial regions where the land features were parallel to the SAR flight line. This dependence on orientation makes this fusion process more ideal for datasets with more consistent features throughout the scene.

Future ways to expand on this work include using higher spatial resolution SAR data and adjusting the weight of the SAR data in the fusion process. Increased spatial resolution for the SAR data will provide more detail for some of the finer regions of interest. For example, the

golf course and road regions are very narrow by design. In some places these regions were as narrow as five to ten meters. In the original SAR data (before resampling during registration) these regions would have been one to two pixels wide. Because SAR data describes texture and geometry of surface features regions of interest should ideally be larger. Another reason that the fusion of the SAR data may have had insignificant effects on classification may have been the weight of the data in the classification algorithm. Because all algorithms used in this work weigh each dimension of the vector to be classified equally, the SAR data contributed less than half of the weight of the WV-2 data to the final vector (three dimensions versus eight respectively). Giving the SAR data more weight in the classification process would increase the impact in the results of the additional data.

APPENDIX: ADDITIONAL RESULTS FIGURES AND TABLES

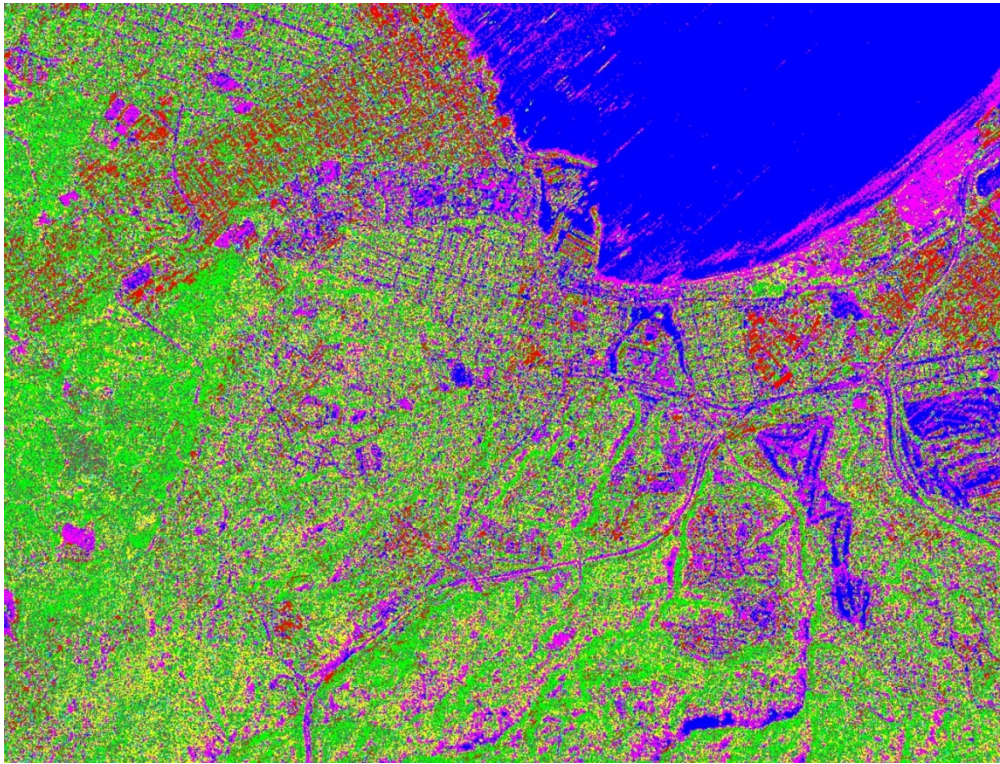


Figure 20. SAR Mahalanobis distance classification

Predicted Class	Reference Class								Total
	1	2	3	4	5	6	7	8	
1	36.55	0	1.22	0.28	1.37	0	2.64	0.05	7.6
2	4.58	100	0.74	65.12	30.36	10.46	39.76	4.79	43.39
3	16.04	0	46.12	0.34	0.94	0	4.58	12.54	10.86
4	9.84	0	18.3	2.09	1.77	1.79	4.71	16.49	6.54
5	6.04	0	4.59	1.12	0.69	0	4.58	6	2.72
6	4.56	0	1.44	28.93	62.81	87.75	34.79	23.46	16.65
7	14.78	0	5.85	1.28	0.72	0	6.91	13.58	5.44
8	7.6	0	21.74	0.84	1.34	0	2.03	23.08	6.8
Total	100	100	100	100	100	100	100	100	100

Table 20. SAR Mahalanobis distance confusion matrix

Class	Prod. acc.	User acc.
1	36.55	94.63
2	100	75.41
3	46.12	57.38
4	2.09	2.9
5	0.69	1.56
6	87.75	34.16
7	6.91	6.44
8	23.08	31.26

Table 21. SAR Mahalanobis distance user/prod. acc.

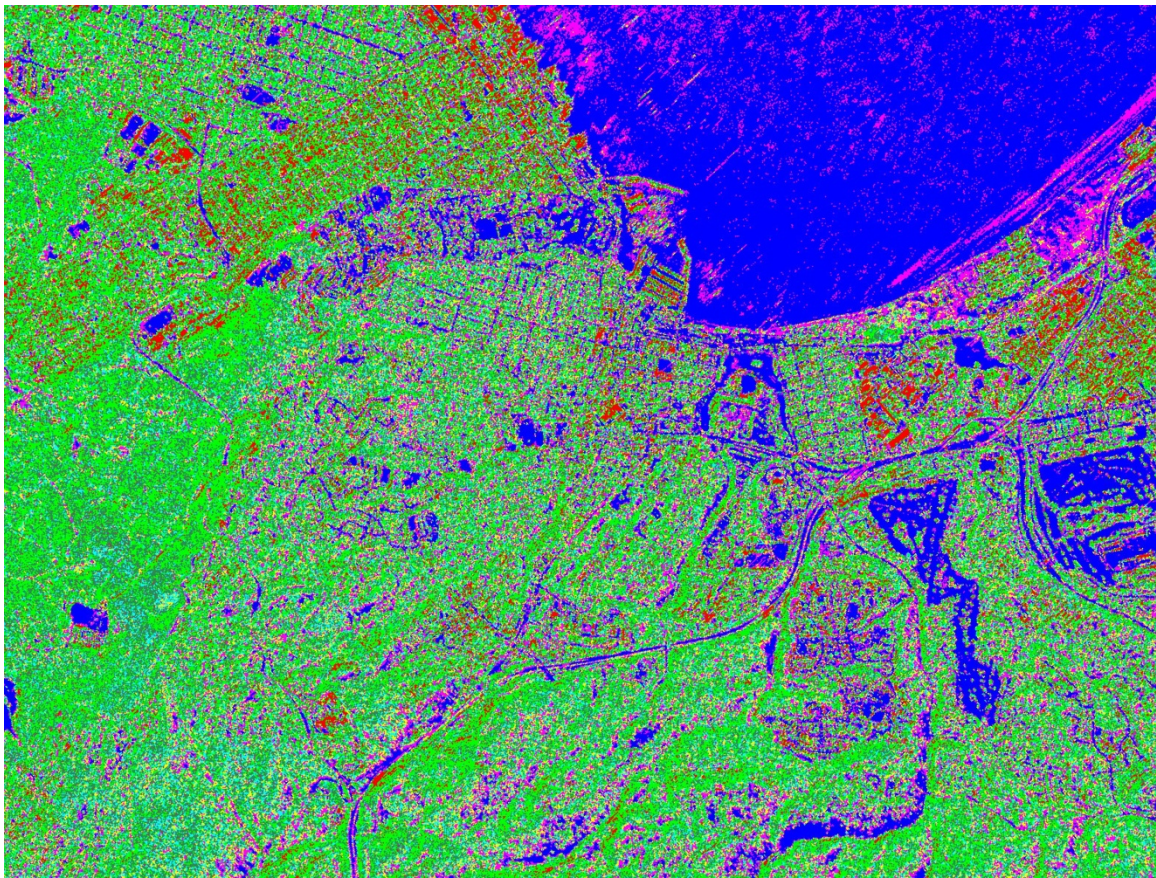


Figure 21. SAR minimum distance classification image

Predicted Class	Reference Class								Total
	1	2	3	4	5	6	7	8	
1	33.84	0	1.59	0.25	0.4	0	1.23	0	6.98
2	1.35	89.92	0.38	87.84	84.24	64.11	59.14	13.34	49.61
3	28.11	0	47.94	0.9	2.39	0	9.47	18.01	14.36
4	6.97	0	4.89	2.43	1.55	1.89	4.27	7.38	3.32
5	7.76	0	14.35	0.62	0.51	0	5.55	14.04	5.12
6	7.69	10.08	1.17	6.42	8.93	34	15.72	14.02	10.27
7	3.06	0	2.56	0.31	0.54	0	2.25	4.65	1.55
8	11.22	0	27.12	1.22	1.45	0	2.38	28.55	8.8
Total	100	100	100	100	100	100	100	100	100

Table 22. SAR minimum distance confusion matrix

Class	Prod. acc.	User acc.
1	33.84	95.43
2	89.92	59.31
3	47.94	45.1
4	2.43	5.24
5	0.51	0.61
6	34	21.45
7	2.25	7.36
8	28.55	29.89

Table 23. SAR minimum distance user/prod. acc.

THIS PAGE INTENTIONALLY LEFT BLANK

LIST OF REFERENCES

- Alparone, L., Baronti, S., Garzelli, A., & Nencini, F. (2004). Landsat ETM+ and SAR image fusion based on generalized intensity modulation. *IEEE Transactions on Geoscience and Remote Sensing*, 42(12), p. 2832-2839.
- Amrinder. (2012). *Confusion matrix - another single value metric - kappa statistic*. Retrieved July 30, 2012, from <http://standardwisdom.com/softwarejournal/2011/12/confusion-matrix-another-single-value-metric-kappa-statistic/>
- Carper, W., Lillesand, T., & Kiefer, R. (1990). The use of intensity-hue-saturation transformations for merging SPOT panchromatic and multispectral image data. *Photogrammetric Engineering and Remote Sensing*, 56, 459-467.
- Chai, C. (2011). *Imaging ellipsometry - principles of operation for surface characterization*. Retrieved 8/30, 2012, from <http://www.azonano.com/article.aspx?ArticleID=2944>
- Chapman, B. D. (2010). *UAVSAR - home*. Retrieved May 15, 2012, from <http://uavsar.jpl.nasa.gov/>
- Cloude, S. R., & Pottier, . (1996). A review of target decomposition theorems in radar polarimetry. *Transactions on Geoscience and Remote Sensing*, 34(2), 498-518.
- Cloude, S. R. (1985). Target decomposition theorems in radar scattering. *Electronics Letters*, 21(1), 22-24.
- Cohen, J. (1960). A coefficient of agreement for nominal scales. *Educational and Psychological Measurement*, 20(1), 37-46.
- Congalton, R. G. (1991). A review of assessing the accuracy of classification of remotely sensed data. *Remote Sensing of Environment*, 37(1), 35-46.
- Cooley, T. (2002). FLAASH, a MODTRAN4-based atmospheric correction algorithm, its application and validation. *Geoscience and Remote Sensing Symposium, 2002. IGARSS '02*, 3, 1414-1418.

- DigitalGlobe. (2009). *WorldView-2* | DigitalGlobe. Retrieved 06/13, 2012, from <http://worldview2.digitalglobe.com/>
- Elachi, C. (1987). *Introduction to the physics and techniques of remote sensing*. Hoboken, NJ: John Wiley & Sons.
- ENVI software | image processing and analysis solutions from exelis*. (2012). Retrieved June 7, 2012, from <http://www.exelisvis.com/ProductsServices/ENVI.aspx>
- Fried, D. L. (1966). Limiting resolution looking down through the atmosphere. *Journal of the Optical Society of America*, 56(10), 1380-1384.
- Graves, C. D. (1956). Radar polarization power scattering matrix. *Proceedings of the IRE*, 44(2), 248-252.
- Guindon, B., Harris, J. W. E., Teillet, P. M., Goodenough, D. G., & Meunier, G. F. (1980). Integration of MSS and SAR data of forested regions in mountainous terrain. *Proceedings of the Fourteenth International Symposium on Remote Sensing of Environment*, 3, 1673-1682.
- Gupta, R. P. (1991). *Remote sensing geology*. Heidelberg, Germany: Springer-Verlag.
- Harris, J., & Murray, R. (1989). IHS transform for the integration of radar imagery with geophysical data. *Proceedings of IGARSS 1989 and Canadian Symposium on Remote Sensing*, 2, 923-926.
- Hartigan, J. A., & Wong, M. A. (1979). A K-means clustering algorithm. *Journal of the Royal Statistical Society. Series C (Applied Statistics)*, 28(1), 100-108.
- Haydn, R., Dalke, G., Henkel, J., & Bare, J. (1982). Application of the IHS color transform to the processing of multisensor data and image enhancement. *Remote Sensing of Arid and Semi-Arid Lands, Proceedings of International Symposium*, , 599-607.
- Hoffer, R. M. (1995). Combination of Landsat TM and ERS-1 satellite data to discriminate forest cover types in brazil. *Multispectral and Microwave Sensing of Forestry Hydrology, and Natural Resources*, Mouglin, Ranson, and Smith, SPIE, Volume 2314,

- Huynen, J. R. (1990). Stokes matrix parameters and their interpretation in terms of physical target properties. *Proceedings of the Journées Internationales De La Polarimétrie Radar (JIPR '90)*, Nantes, France.
- Huynen, J. R. (1965). Measurement of the Target scattering matrix. *Proceedings of the IEEE*, 53(8), 936.
- Jensen, J., & Lulla, K. (1987). In Prentice Hall (Ed.), *Introductory digital image processing: A remote sensing perspective* (1st ed.) Upper Saddle River, NJ: Prentice Hall.
- Kempeneers, P., Sedano, F., Seebach, L., Strobl, P., & San-Miguel-Ayanz, J. (2011). Data fusion of different spatial resolution remote sensing images applied to forest-type mapping. *IEEE Transactions on Geoscience and Remote Sensing*, 49(12), 4977-4986.
- Kleeman, R. D. (1930). Electromagnetic radiation and the properties of the electron. *Science, New Series*, 72(1861), 225-226.
- Kruse, F. A. (2004). Comparison of ATREM, ACORN, and FLAASH atmospheric corrections using low-altitude AVIRIS data of Boulder, CO. *Summaries of 13th JPL Airborne Geoscience Workshop, Jet Propulsion Lab, Pasadena, CA*.
- Leckie, D. G. (1990). Synergism of synthetic aperture radar and Visible/Infrared data for forest type discrimination. *Photogrammetric Engineering and Remote Sensing*, 56(9), 1237-1246.
- Lee, J., & Pottier, E. (2009). *Polarimetric radar imaging: From basics to applications* (1st ed.). Boca Raton, FL: CRC Press/Taylor and Francis Group.
- Liu, J., Tian, J., Sang, H., & Ma, J. (2011). Fusion of airborne SAR image and color aerial image for land use classification. *Remote Sensing Image Processing, Geographic Information Systems, and Other Applications*, 8006, 80060F-80060F-5.

- MacDonald, J. (1999). *The new generation of earth observation spacecraft and its impact on operationalization*. Retrieved August 30, 2012, from http://www.elektronik-service.ch/new_generation_of_earth_observat.htm
- Marchisio, G. (2010). On the relative predictive value of the new spectral bands in the WorldView-2. *Geoscience and Remote Sensing Symposium (IGARSS), 2010*, , 2723-2726.
- Matthew, M. W., Alder-Golden, S. M., & Berk, A. (2002). Atmospheric correction of spectral imagery: Evaluation of the FLAASH algorithm with AVIRIS DATA. *Applied Imagery Pattern Recognition Workshop, 2002. Proceedings. 31st*, pp. 157-163.
- McLachlan, G. J. (1999). Mahalanobis distance. *Resonance - Journal of Science Education*, 4(6), 20-26.
- Mohd, H., Pakhriazad, H. Z., & Shahrin, M. F. (2009). Evaluating supervised and unsupervised techniques for land cover mapping using remote sensing data. *Malaysian Journal of Society and Space*, 5(1), 1-10.
- Monserud, R. A., & Leemans, R. (1992). Comparing global vegetation maps with the kappa statistic. *Ecological Modelling*, 62(4), 275-293.
- Olsen, R. C. (2007). *Remote sensing from air and space* (First ed.). Bellingham, WA: SPIE International Society for Optical Engineering.
- Pohl, C., & Van Genderen, L. (1998). Review article multisensor image fusion in remote sensing: Concepts, methods, and applications. *International Journal of Remote Sensing*, 19(5), 823-854.
- Prakash, R., & Singh, D. (2012). A fusion approach to retrieve soil moisture with SAR and optical data. *IEEE Journal of Selected Topics in Applied Earth Observations and Remote Sensing*, 5(1), 196-206.
- Richards, J. A. (2005a). Analysis of remotely sensed data: The formative decades and the future. *IEEE Transactions on Geoscience and Remote Sensing*, 43(3), 422-432.

- Richards, J. A. (2005b). *Remote sensing: Digital image analysis* (4th ed.). Germany: Springer.
- Robertson, T. V. (1973). Extraction and classification of objects in multispectral images. *Proceedings of the Conference on Machine Processing of Remotely Sensed Data, Purdue University, West Lafayette, IN.* pp. 27-34.
- Sah, S., van Aardt, J., Mckeown, D., & Messinger, D. (2012). A multi-temporal analysis approach for land cover mapping in support of nuclear incident response. *Algorithms and Technologies for Multispectral, Hyperspectral, and Ultraspectral Imagery XVIII, Proceedings of SPIE, , 8390.* pp. 83900C-1-83900C-7.
- Smedes, H. W., Hulstrom, R. L., & Ranson, K. J. (1975). The mixture problem in computer mapping of terrain: Improved techniques for establishing spectral signature, atmospheric path radiance, and transmittance. *NASA LBJ Space Center Earth Resources Surv. Symp., 1-B,* 1099-1159.
- Strahler, A. H. (1980). The use of prior probabilities in maximum likelihood classification of remotely sensed data. *Remote Sensing of Environment, 10(2),* 135-163.
- Thunig, H., Wolf, N., Naumann, S., Siegmund, A., Jurgens, C., Uysal, C., et al. (2011). Land use/ land cover classification for applied urban planning - the challenge of automation. *Urban Remote Sensing Event (JURSE), 2011 Joint,* pp. 229-232.
- Tomiyasu, K. (1978). Tutorial review of synthetic-aperture radar with applications to imaging of the ocean surface. *Proceedings of the IEEE, 66(5),* 563-583.
- Turner, R. E. (1975). *Atmospheric effects in multispectral remote sensor data* No. ERIM 109600-15-F)Environmental Research Institute of Michigan, Ann Arbor.
- Tyo, J. S., Golstein, D. L., Chenault, D. B., & Shaw, J. A. (2006). Review of passive imaging polarimetry for remote sensing applications. *Applied Optics, 45(22),* 5453-5469.
- Vanzyl, J., Zebker, H., & Elachi, C. (1987). Imaging radar polarization signatures - theory and observation. *Radio Science, 22(4),* 529-543.

- Wacker, A. G., & Landgrebe, D. A. (1971). *The minimum distance approach to classification* No. 100771). School of Electrical Engineering Purdue University Lafayette, Indiana: Laboratory for Applications of Remote Sensing.
- Wacker, A. G., & Landgrebe, D. A. (1972). Minimum distance classification in remote sensing. *Proceedings of the 1st Canadian Symposium on Remote Sensing, 2*, 577.
- Ward, S. H., & Smith, B. D. (1974). On the computation of polarization ellipse parameters. *Geophysics, 39*(6), 867-869.
- Wu, S. T. (1982). Multisensor data analysis and its application to monitoring of cropland, forest, strip mines, and cultural targets. *Machine Processing of Remotely Sensed Data Symposium, July, 1982*,
- Zhang, L., Zhang, J., Zou, B., & Zhang, Y. (2008). Comparison of methods for target detection and applications using polarimetric SAR image. *Progress in Electromagnetic Research, PIERS Online, 4*(1), 140-145.

INITIAL DISTRIBUTION LIST

1. Defense Technical Information Center
Ft. Belvoir, Virginia
2. Dudley Knox Library
Naval Postgraduate School
Monterey, California
3. Fred A. Kruse
Naval Postgraduate School
Monterey, California
4. D. C. Boger
Naval Postgraduate School
Monterey, California
5. R. C. Olsen
Naval Postgraduate School
Monterey, California